Structural relaxation dynamics of electronically excited $XeAr_N$ clusters

Alexander Goldberg and Joshua Jortner[a)]
School of Chemistry, Tel-Aviv University, Ramat Aviv, 69978 Tel Aviv, Israel

(Received 4 April 1997; accepted 15 August 1997)

In this article we explore the structural, dynamic, and spectroscopic implications of large local configurational changes in electronically excited Xe^*Ar_N ($N=12,54,146,199$) heteroclusters, where the Xe* [$\equiv Xe(^3P_1)$] atom is excited to the lowest dipole-allowed extravalence Rydberg excitation. The ultrafast femtosecond and picosecond dynamics driven by the short-range repulsive interaction between the vertically excited Xe* Rydberg and the cluster Ar atoms was studied by molecular dynamics simulations. From the analysis of the time dependence of the structural parameters for site-specific Xe excitations in medium-sized ($N=54$) and large ($N=146,199$) clusters, two general configurational relaxation phenomena were established: a ''bubble'' formation (i.e., a large configurational dilation around Xe*) for Xe interior sites and a ''spring'' formation (i.e., the stretching of Xe* outside the cluster) for Xe surface sites. General Xe site-specific features of both bubble and spring formation involve ultrashort (Gaussian) energy transfer to the cluster ($\sim 50-100$ fs characteristic times τ_{ET}) inducing configurational relaxation, which manifests a multimodal time solution. The initial (Gaussian) temporal mode ($\sim 150-300$ fs characteristic times $\tau_0 > \tau_{ET}$) is followed by an exponential mode (ps lifetime τ_1), with subsequent impact induced, damped vibrational coherence effects with frequencies (ω_2, ω_3), and exponential decay (ps lifetimes τ_2, τ_3). The bubble formation for the central site of Xe^*Ar_{146} or Xe^*Ar_{54} is induced by energy transfer of $\tau_{ET} \cong 60$ fs followed by subsequent multimodal dilation with $\tau_0 \cong 170$ fs and $\tau_1 \cong 2$ ps, and a subsequent expansion with coherent motion of vibrational wave packets with $\omega_2, \omega_3 \cong 20$, 40 cm^{-1} and $\tau_2, \tau_3 \cong 2$, 6 ps. The bubble reaches an equilibrium configuration after ~ 10 ps with asymptotic spatial expansion of $\Delta R_b^* = 0.7-0.8$ Å. The spring formation for an exterior surface site of Xe^*Ar_{146} is $\tau_{ET} \cong 80$ fs and $\tau_0 \cong 210$ fs, which is followed by a substantial ($\cong 1.2$ Å) Xe* stretching and a subsequent contraction accompanied by vibrational coherence effects with $\omega_2 \cong 10$ cm^{-1} and $\tau_2 \cong 20$ ps, with the asymptotic spring spatial extension $\Delta R_s^* \cong 0.6$ Å, being accomplished after ~ 30 ps. Regarding dynamic cluster size effects we established that following vertical excitation at initial temperatures $T_i = 10-30$ K, the following phenomena are manifested: (i) Large Xe^*Ar_{146} and Xe^*Ar_{199} clusters exhibit short-time (10–20 ps) configurational relaxation in rigid clusters. (ii) The central site in a medium-sized Xe^*Ar_{54} cluster undergoes a rigid–nonrigid (''melting'') transition induced by the electronic excitation, with the Xe* manifesting long-time (100–200 ps) mass transport from the interior bubble to the surface spring. (iii) Small Xe^*Ar_{12} clusters exhibit stepwise reactive dissociation on the ps time scale. The spectroscopic implications of large configurational relaxation in Xe^*Ar_N ($N=54,146$) clusters were interrogated by the simulations of the Xe site-specific time-dependent spectral shifts in emission, which decrease from the initial large values [e.g., $\delta\nu_e(t=0) = 0.92$ eV at $T_i = 10$ K for the central site] to low values. The time evolution of the emission spectral shifts is qualitatively similar to the structural dynamics, which involves initial ultrafast ($\sim 50-100$ fs) decay, a (ps) exponential contribution, and a damped oscillatory behavior. The time-resolved Xe site-specific emission spectral shifts obey an exponential structure-spectral relationship which is isomorphous with time-independent relations for the absorption spectral shifts and for the emission asymptotic spectral shifts. Finally, predictions are provided for the spectroscopic interrogation (by energy-resolved fluorescence) of the longer time (~ 150 ps) Xe* bubble mass transport in nonrigid Xe^*Ar_{54} clusters. The long-time fluorescence spectra, which were simulated by the spectral density method, exhibit: (i) A Gaussian line shape, corresponding to the slow modulation limit. (ii) Spectral shifts ($\langle \delta\nu_e \rangle = 0.01-0.1$ eV) exhibiting a site-specific hierarchy, i.e., $\langle \delta\nu_e \rangle$(central) $> \langle \delta\nu_e \rangle$(interior) $> \langle \delta\nu_e \rangle \times$(surface) $> \langle \delta\nu_e \rangle$(top). (iii) Linewidths (full width at half-maximum) which follow the order of the site-specific hierarchy of the spectral shifts. The calculated site-specific emission spectral shifts and linewidths and the calculated Stokes shifts for central and interior bubble sites and for surface spring sites in Xe^*Ar_{146} are in reasonable agreement with the experimental results for Xe^*Ar_{1400} clusters. Our overall picture regarding the dynamic and spectroscopic implications of large excited-state configurational relaxation provides guidance, predictions, and insight for the fate of Rydberg states in clusters and in the condensed phase. © *1997 American Institute of Physics.* [S0021-9606(97)03843-9]

[a)]Electronic mail: jortner@chemsgl.tau.ac.il

I. INTRODUCTION

One of the unique characteristics of clusters pertains to their size-dependent large surface/volume ratio.[1–6] Structural considerations,[4] in conjunction with exciton spectroscopy of neat rare-gas clusters by Möller *et al.*[7] have confirmed the prediction of the liquid drop model[8] that in a Kr_N cluster containing N constituents the fraction F of surface constituents is $F \propto n^{-1/3}$. Subsequent studies by Möller *et al.*[9,10] provided rich information on the spectroscopy of surface and interior Frenkel, Wannier, and core excitons in neat Ar_N clusters. Of course, the segregation between internal and surface sites provides only coarse grained information. Different energetic and spectroscopic observables will be exhibited for distinct substitutional sites of an atomic impurity in an elemental atomic heterocluster. Experimental[7,11–14] and theoretical[15] studies provided an identification of distinct surface and interior sites in $XeAr_N$ clusters on the basis of the electronic absorption spectra of the guest atom. The energetics of the lowest dipole allowed extravalence electronic excitation of a Xe atom in $XeAr_N$, i.e., $^1S_0 \rightarrow {}^3P_1({}^2P_{3/2}6s[3/2]_1)$ (which will be denoted by Xe*) constitutes a sensitive probe for the local microenvironment of the Xe atom in the heterocluster.[11–15] The spectral shift $\delta\nu$ for the optical absorption of Xe in the elemental heterocluster (relative to the isolated atom) is dominated by large short-range Xe Rydberg state-cluster host atoms repulsive interactions, resulting in a large blue spectral shift towards higher energies.[15–19] The cluster-size-dependent spectroscopic observables reveal an analogue to an atomic shell structure with a hierarchy of Xe occupied site-specific spectral shifts in absorption, decreasing in the order[15] $\delta\nu$(central site) $>\delta\nu$(interior site)$>\delta\nu$(surface sites)$>\delta\nu$(top atom), providing a spectroscopic method for the interrogation of the site-specific local structure.[15] The theoretical[15–20] and experimental[11–14,16–19] information on the energetics, manifested by $\delta\nu$, and on the nuclear dynamics, emerging from the homogeneous absorption line shape,[15,20] provide the basis for the exploration of excited-state dynamics of $XeAr_N$ clusters.

The dominance of the short-range excited-state repulsive Xe*–Ar interactions in the nuclear configuration space, which is accessible by vertical excitation from the equilibrium ground state, has profound dynamic implications. One expects this repulsive interaction to induce a significant increase in the (mean) equilibrium Xe*–Ar distances in the electronically excited state relative to the Xe–Ar distances in the ground electronic state. These general considerations were borne out by the molecular dynamics (MD) studies of Scharf, Landman, and Jortner[21,22] on interior and surface configurations of the electronically excited Xe^*Ar_{12} and Xe^*Ar_{54} clusters. In this article we explore ultrafast femtosecond and picosecond cluster dynamics driven by an extravalence electronic excitation. Brief preliminary reports on excited state structural relaxation dynamics in Xe^*Ar_{146} clusters were already presented by us.[6,23] We report on the nuclear dynamics and on the spectroscopic implications of large excited-state configurational changes in Xe^*Ar_N ($N=12-200$) clusters. The time-resolved femtosecond and picosecond dynamics of structural changes for site-specific Xe excitations were studied by MD simulations. From the analysis of time-dependent configurational parameters for these heteroclusters two general effects were documented:

(1) The ''spring'' formation for a surface Xe* atom. This is manifested by the stretching out of Xe* to a larger equilibrium distance from the surface.
(2) The ''bubble'' formation for the interior Xe* atom. A large configuration dilation is exhibited around the local Rydberg impurity excitation.

To make contact between the configurational relaxation and experimental observables we have investigated the time-dependence of the fluorescence spectra and of the Stokes shifts between the peaks of the emission and of the absorption bands. Finally, the semiclassical spectral density method[15,20,24–41] was applied for MD simulations of the emission spectra of Xe^*Ar_N clusters from the vibrationally equilibrated electronically excited state on the nanosecond time scale, which were confronted with experimental energy-resolved spectroscopic results.[11]

II. SIMULATIONS

A. Potential parameters

The ground state Ar–Ar and Xe–Ar pair potentials were modeled by the Lennard–Jones (LJ) form with the parameters: $\sigma_{Ar-Ar}=3.405$ Å, $\epsilon_{Ar-Ar}=0.0103$ eV, $\sigma_{Xe-Ar}=3.65$ Å, and $\epsilon_{Xe-Ar}=0.0153$ eV.[15,42–44] The appropriate choice of the excited-state $Xe^*({}^3P_1)-Ar({}^1S_0)$ potential is crucial. We have used the exp-6 potential derived by Messing, Raz, and Jortner[16,17] from a detailed and satisfactory fit of the absorption spectra of Xe in fluid Ar over a broad density range from the low-pressure gas phase up to the liquid. This pair potential is of the form[16,17]

$$V_{Xe^*-Ar}(r)=\epsilon(1-6/\alpha)^{-1}\{(6/\alpha)\ \exp[\alpha(1-r/r_e)] - (r_e/r)^6\}, \quad (1)$$

with the parameters $\epsilon=0.008$ eV, $r_e=4.65$ Å, and $\alpha=15$. Messing *et al.*[16–18] have found that the exp-6 excited-state potential (Eq. 1) is superior to the LJ potential in accounting for the density and temperature dependence of the absorption spectra of Xe in fluid Ar over a broad density range. We have assessed the sensitivity of the simulated absorption spectra of $XeAr_N$ ($N=12$, 54, 146) clusters to the form of the excited-state potential, showing that the spectral shifts and the linewidths calculated with the excited-state LJ potential are systematically lower by about 30% than those obtained with the exp-6 potential (Eq. 1).[15] The absorption spectral shifts for $XeAr_{146}$ clusters at the experimental temperature domain 25–35 K,[15] calculated with the exp-6 potential (but not with the LJ excited-state potential),[15] are in good agreement with experiment.[9,11] The exp-6 potential, Eq. (1), will be used in our calculations of the excited-state dynamics and of fluorescence spectroscopy.

B. Molecular dynamics in the electronically excited state

We performed constant energy MD simulations[45] using the Nordsieck fifth-order algorithm to integrate the classical equations of motion (time step 2–5 fs). A vertical electronic excitation from the equilibrated ground state potential surface $V_g\{\mathbf{r}_A(t)\}$ to the electronically excited state potential $V_e\{\mathbf{r}_A(t)\}$ [where $\mathbf{r}_A(t)$ are the nuclear coordinates of the $A=1,...,(N+1)$ atoms] was performed, followed by the interrogation of the nuclear dynamics on the V_e potential surface. The procedure is based on the following steps:

(i) Characterization of initial ground state structures. The initial structures were characterized by using the conjugate gradient method[46,47] on the ground-state potential surface. Doped $XeAr_N$ ($N=12$, 54, 146) icosahedra[48] were prepared at $T=10$ K and 30 K, with the Xe atom being substituted into each of the nonequivalent sites.[15] $XeAr_{199}$ clusters were prepared by removing Ar atoms from the outer shell of the $N=309$ Mackay icosahedron.

(ii) Sampling of initial configurations on V_g for the vertical excitation. The thermal equilibration procedure of an initial structure at the temperatures $T=10$ K and $T=30$ K on the ground-state potential surface was carried out by the iterative scaling of the velocities.[45] Subsequently, a constant energy trajectory was generated on V_g for 1 ns. From this trajectory 100 initial, statistically independent, points in the configuration space were sampled, serving as the initial nuclear configurations on V_e.

(iii) Structural parameters for electronically excited states with the 100 independently sampled initial configurations. We calculated ensemble averaged structural and spectroscopic time-resolved observables for the electronically excited Xe^*Ar_N clusters. Each point was averaged over 100 excited-state trajectories (for $t \leqslant 20$ ps) and over 10 excited-state trajectories for ($t=20-1000$ ps).

The following structural parameters were useful for the specification of the nuclear dynamics in the electronically excited state.[15,21,22]

(a) $R^*_{CM}(t)$. The distance between the Xe* atom and the center of the mass of the $XeAr_N$ cluster.

(b) $NN^*(t)$. The average number of Ar atoms in the nearest-neighbor positions to Xe*. We have used the criterion[15,49] that any Ar atom with an Xe*–Ar distance of $\leqslant 1.15\ r_e$ (where $r_e=4.65$ Å is the equilibrium Xe*–Ar separation) counts as a nearest-neighbor atom.

(c) $R^*_{NN}(t)$. The average distance between Xe* and the first coordination shell of Ar atoms, i.e.,

$$R^*_{NN}(t)=[NN^*(t)]^{-1}\sum_{j=1}^{NN^*(t)}|[\mathbf{R}_j(t)-\mathbf{R}_{Xe^*}(t)]|, \qquad (2)$$

where $\mathbf{R}_{Xe^*}(t)$ and $\mathbf{R}_j(t)$ are the position vectors of the Xe* atom and of the nearest-neighbor Ar atoms, respectively.

We note that all the three structural parameters $R^*_{CM}(t)$, $NN^*(t)$, and $R^*_{NN}(t)$ are time dependent with $t=0$ being characterized by the vertical excitation.

The cluster vibrational energy after the vertical excitation was specified by the kinetic energy $KE=\Sigma_{i=1}^{N} m_i\mathbf{v}_i^2/2$ via the cluster temperature

$$T=2KE/(3N-6)k_B, \qquad (3)$$

where N is the number of atoms in the cluster, m_i is the mass of the ith atom, and $\mathbf{v}_i$ its velocity. The cluster temperature ($T\propto KE$) was defined as though the system satisfies the principle of detailed balance due to the small time step (2–5 fs) employed in the simulations.

C. Time-resolved emission

An important spectroscopic implication of the configuration relaxation in the electronically excited state of Xe^*Ar_N pertains to the time-resolved spectral shift $\delta\nu_e(t)$ in emission, which can be specified in terms of the time-dependent first moment[50–52] $M_1^e(t)$ of the $Xe^*(^3P_1)Ar_N \rightarrow Xe(^1S_0)Ar_N$ fluorescence, i.e.,

$$M_1^e(t)=V_g(\{\mathbf{r}_A(t)\})-V_e(\{\mathbf{r}_A(t)\}). \qquad (4)$$

The initial configurations for the calculation of Eq. (4) were chosen by the sampling procedure [step (ii) of Sec. (II B)]. The trajectories were subsequently propagated on V_e. Each point in the time domain was obtained by averaging over 10–100 trajectories. For the time domain of 10–25 ps the configurational and the spectroscopic observables were averaged over 100 trajectories. We assessed the convergence of the configurational and spectroscopic observables on the time scale of the radiative lifetime of $Xe^*(^3P_1)$ ($\tau=3-5$ ns [19]). For this purpose, ''long-time'' (1 ns) trajectories were propagated from the initial vertical nuclear configuration on V_e, averaging over 50 independent trajectories for $N=12$ and $N=54$ and over 10 independent trajectories for $N=146$ and $N=199$.

The time-resolved spectral shift in emission relative to the emission (or absorption) of the bare Xe atom is

$$\delta\nu_e(t)=-M_1^e(t), \qquad (4a)$$

which approximately corresponds to the peak of the time-resolved emission spectrum. It will also be useful to define the time-resolved Stokes shift $SS(t)$ between the peak of the time-resolved emission spectrum and the peak of the time-independent absorption spectrum (with the spectral shift $\delta\nu$), i.e.,

$$SS(t)=\delta\nu-\delta\nu_e(t). \qquad (5)$$

The structural parameters $R^*_{CM}(t)$, $R^*_{NN}(t)$, and $NN^*(t)$, together with the spectroscopic parameters $\delta\nu_e(t)$ and $SS(t)$, will provide spectroscopic information on the time-resolved excited-state nuclear dynamics in the cluster. This approach for cluster excited-state dynamics bears a close analogy to the interrogation of time-dependent dynamics in macro-

scopic solvents, e.g., the solvation of an electronically excited giant dipole molecule[53] or of an excess electron in polar solvents[54–56] were explored by ps or fs laser spectroscopy, and by the formation dynamics of the excess electron bubble in liquid helium.[52]

D. Emission line shapes

Energy-resolved total fluorescence line shapes were calculated by a straightforward extension of the spectral density method.[15,20,24–41] These emission line shapes $L_e(E)$, at the emitted photon energy E, were calculated by averaging over the accessible region Ω_e of the phase space at the electronically excited state. These time-independent calculated emission line shapes are obtained from averaging over initial excited-state trajectories. This analysis was performed for Xe^*Ar_N ($N=12$, 54, 146, 199) clusters at two initial temperatures ($T_i=10$ and 30 K) for different substitutional sites of the Xe* atom. To obtain the emission line shapes the following steps were undertaken: (1) propagation of a long trajectory over V_e beginning from the equilibrated ground state trajectory; (2) choosing of 20 initial statistically independent configurations of the excited state. The first point in the configuration space was chosen in 25 ps, which corresponds to the equilibration time on the V_e potential surface; (3) calculation of microcanonical emission spectra; (4) averaging the line shape over the trajectories. This procedure gives a ''long-time'' emission line shape for medium-sized and large clusters, which can be confronted with the experimental energy-resolved emission spectra.[11]

The semiclassical emission line shape for a microcanonical subspectrum is given by[24–31]

$$L_e(E)=\frac{1}{\pi}\,\mathrm{Re}\int_0^\infty dt\,\exp[i(E+\omega_{ge}+\langle U^e\rangle)\tau]\times\exp[-g^e(\tau)], \tag{6}$$

where

$$\langle U^e\rangle=\langle V_g(t)-V_e(t)\rangle \tag{7}$$

is the excited-state time-dependent energy gap, where $\langle\ \rangle$ denotes a trajectory average, ω_{ge} is the 0-0 emission energy of the bare Xe* atom, and $g^e(\tau)$ is the two-time integral of the semiclassical energy-gap autocorrelation function in the time domain, i.e.,

$$g^e(\tau)=\int_0^\tau d\tau_1\int_0^{\tau_1}d\tau_2 J^e_{\mathrm{sc}}(\tau_2). \tag{8}$$

Here $J^e_{\mathrm{sc}}(\tau)=\mathrm{FT}(J^e_{\mathrm{sc}}(\omega))$, where

$$J^e_{\mathrm{sc}}(\omega)=\left[1+\tanh\left(\frac{\hbar\omega}{2k_BT}\right)\right]J_e(\omega), \tag{9}$$

with $J_e(\omega)$ being the Fourier transform (FT), i.e., the power spectrum, of the classical energy gap autocorrelation function

$$J_e(\tau)=\langle U'_e(0)U'_e(\tau)\rangle, \tag{10}$$

with $U'_e(\tau)=V_g(\tau)-V_e(\tau)-\langle U^e\rangle$.

The averaged semiclassical emission line shape $\overline{L_e}(E)$ is given by

$$\overline{L_e}(E)=\frac{1}{\pi}\,\mathrm{Re}\int_{\Omega_e}dp\,dq\int_0^\infty d\tau\rho_e(q,p,\tau)\times\exp[i(E+\omega_{ge}+\langle U^e\rangle)\tau]\exp[-g^e(\tau,p,q)], \tag{11}$$

where q and p are the coordinates and momenta of the atoms and $\rho_e(q,p,t)$ is the distribution function in the electronically excited state in the accessible region Ω_e of the phase space. The averaging over Ω_e was conducted by ensemble averaging over 20 microcanonical spectra, each obtained using a 1 ns trajectory.

E. Moments of the emission spectra

The emission line shapes were characterized in terms of the long-time (1 ns) first moment M_1^e and second moment M_2^e of the emission band, which are given by

$$M_1^e=\langle V_g(t)-V_e(t)\rangle \tag{12}$$

and

$$M_2^e=\langle[V_g(t)-V_e(t)]^2\rangle. \tag{13}$$

An analysis of the power spectra $J_e(\omega)$ for the emission of Xe^*Ar_N clusters demonstrates that these systems correspond to the Kubo slow modulation limit.[51] Accordingly, the emission line shape is Gaussian with the emission spectral shift $\langle\delta\nu_e\rangle$ being given in this limit by

$$\langle\delta\nu_e\rangle=M_1^e \tag{14}$$

and the Stokes shift is

$$\langle\mathrm{SS}\rangle=\delta\nu-\langle\delta\nu_e\rangle. \tag{15}$$

We distinguish between the time-dependent first moment $M_1^e(t)$, the spectral shift $\delta\nu_e(t)$, Eq. (4), and their corresponding asymptotic (time-independent) values M_1^e and $\langle\delta\nu_e\rangle$, Eqs. (12) and (14). The emission linewidth [full width at half-maximum (FWHM)] Γ_e is given in the slow modulation limit[51] by the central second moment of the line shape

$$\Gamma_e=2.355[M_2^e-(M_1^e)^2]^{1/2}. \tag{16}$$

Indeed, a direct calculation of the FWHM of the linewidth, Eq. (11), is in good agreement (i.e., within 5%) with Eq. (16). The spectroscopic information for the emission spectra is characterized by the two observables $\langle\delta\nu^e\rangle$ and Γ_e. Similarly, we have previously shown[15] that the Gaussian absorption spectra of $XeAr_N$ are characterized by the spectral shifts $\delta\nu$ and the linewidths (FWHM) Γ of the absorption line shape.

III. STRUCTURAL RELAXATION IN LARGE Xe^*Ar_N CLUSTERS

We have investigated the time evolution of the structural parameters $R^*_{\mathrm{NN}}(t)$, $R^*_{\mathrm{CM}}(t)$, and $\mathrm{NN}^*(t)$ for seven Xe atom substitutional sites in the Xe^*Ar_{146} cluster, which are labeled as in our previous work,[15] in the following manner: (C) cen-

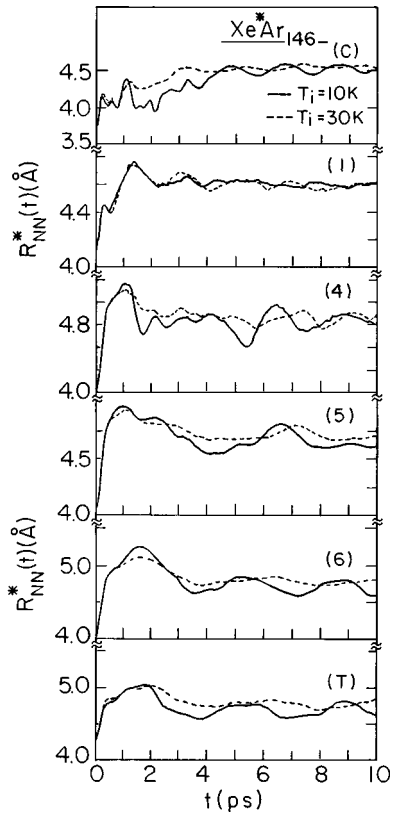

FIG. 1. The site-specific time dependence of the structural parameter $R^*_{NN}(t)$, the average distance between Xe* and the first coordination shell of Ar atoms, for Xe^*Ar_{146} clusters. The substitutional sites are marked on the panels. Data are given for two different initial temperatures $T_i=10$ and $T_i=30$ K.

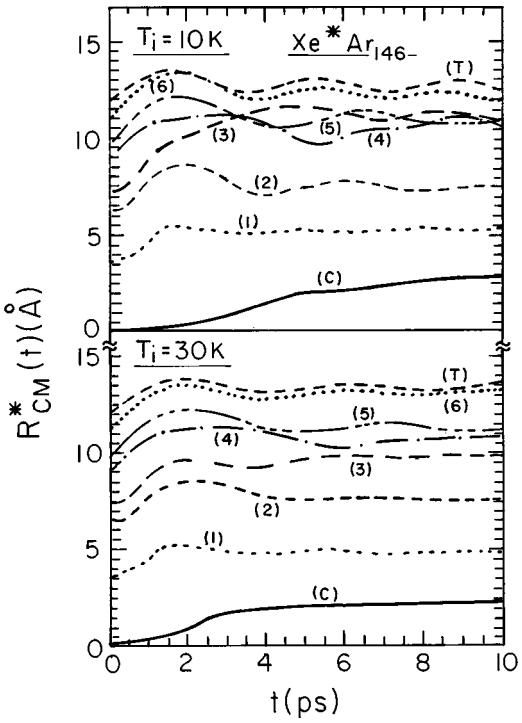

FIG. 2. The site-specific time dependence of the distance $R^*_{CM}(t)$ between the Xe* and the center of mass of the cluster for different initial Xe* substitutional sites (marked on the curves) in the Xe^*Ar_{146} cluster. Initial temperatures are (a) 10 K and (b) 30 K.

ter; (1), (2), and (3) inequivalent sites in the inner sphere; (4), (5), and (6) inequivalent sites in the outer sphere. We have also studied the top (T) Xe* atom. There are four interior sites, i.e., (C), (1), (2), and (3) and four surface sites, i.e., (4), (5), (6), and (T). Vertical electronic excitation of the cluster (whose initial ground-state temperatures are $T_i=10$ K or $T_i=30$ K) results in marked configuration changes on the 10 ps time scale, as evident from the time evolution of $R^*_{NN}(t)$ (Fig. 1), $R^*_{CM}(t)$ (Fig. 2), and $NN^*(t)$ (Fig. 3). Of interest is also the time-dependent cluster temperature $T^*(t)$ (Fig. 4). On a long-time scale $t>20$ ps (i.e., $t=20-1000$ ps) the configuration parameters assume average constant values. The asymptotic values $\langle R^*_{NN}\rangle$, $\langle R^*_{CM}\rangle$, $\langle NN^*\rangle$ and $\langle T^*\rangle$ (averaged over 10 trajectories of 1 ns) are summarized in Table I. From the analysis of the asymptotic values, together with their time dependence, we infer the following:

(a) *The bubble formation around the extravalence excitations in the internal sites (C), (1), (2), and (3).*

(1) Configurational dilation. Following vertical excitation, the $R^*_{NN}(t)$ values increase from their initial value $R^*_{NN}(0)\equiv R_{NN}$, exhibiting a marked configurational dilation around the Rydberg excitation (Fig. 1 and Table I). The average size of the bubble, as measured by $\Delta R^*_b=\langle R^*_{NN}\rangle-R_{NN}$, is $\Delta R^*_b=0.7-0.8$Å for sites (C), (1)–(3) (Table I). The values of ΔR^*_b are nearly (within ± 0.05Å) site independent and independent of the initial temperature (in the range $T_i=10-30$ K).

(2) Multimodal time evolution. The increase of $R^*_{NN}(t)$ from its initial value R_{NN} to the long-time asymptotic value $\langle R^*_{NN}\rangle$ exhibits a multimodal time evolution (Fig. 1).

(3) Overall temporal increase of the bubble size. The

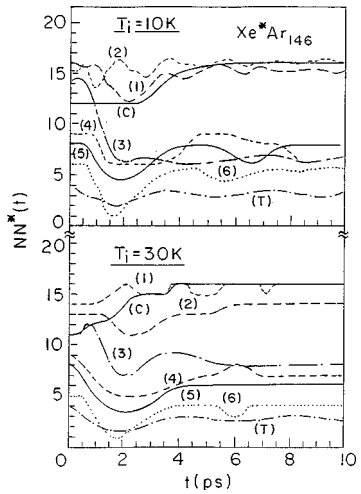

FIG. 3. The time dependence of the number of first nearest neighbors $NN^*(t)$ of the Xe* excited atom in Xe^*Ar_{146} clusters. Different initial Xe* substitutional sites are marked on the curves. Initial temperatures are 10 and 30 K.

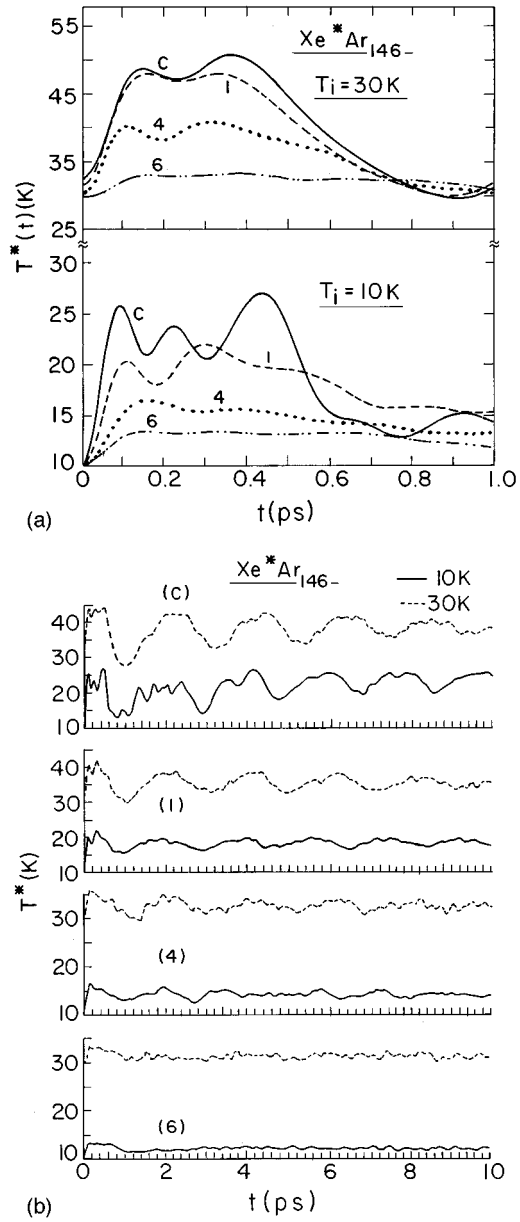

FIG. 4. The time evolution of the cluster temperature $T^*(t)$ for the Xe^*Ar_{146} cluster for different initial Xe* substitutional sites (marked on the curves) for two initial temperatures of $T_i=10$ K and $T_i=30$ K. (a) $t=0-1$ ps. (b) $t=0-10$ ps.

bubble radius increases gradually [apart from the damped oscillations, see paragraph (a)(4)] from the initial value $R^*_{NN}(0)$ to the asymptotic value $\langle R^*_{NN}\rangle$. The relative increase of the bubble radius

$$f(t)=[R^*_{NN}(t)-R^*_{NN}(0)]/[\langle R^*_{NN}\rangle - R^*_{NN}(0)] \qquad (17)$$

is $f(t)<1$ for the (C) site and $f(t)\leqslant 1.1$ for sites (1) and (2), during the entire bubble expansion process.

(4) The bubble expansion manifests damped oscillatory behavior (Fig. 1). The marked temporal oscillations of $R^*_{NN}(t)$ manifest impact induced vibrational coherence resulting from the motion of the bubble. The quantum analogue of this phenomenon constitutes coherence in the motion of a vibrational wave packet of the bubble. The impact induced excitation is characterized by the time scale of $\tau_{ET}\sim 50-60$ fs for initial energy flow into the cluster whose nuclear motion is practically frozen [see paragraph (a)(10)]. The corresponding energy scale is $\hbar/\tau_{ET}\cong 100\ \mathrm{cm}^{-1}$, being sufficiently large to span the energy range of the cluster frequencies and to excite a vibrational wave packet.

(5) The analysis of the dynamics of the bubble formation should account for the multimodal time evolution and for the nuclear vibrational oscillations. We defined the configurational relaxation function

$$F(t)=R^*_{NN}(t)-\langle R^*_{NN}\rangle. \qquad (18)$$

Configurational relaxation for bubble formation was described in terms of a superposition

$$F(t)=A_0\exp(-t^2/2\sigma^2)+A_1\exp(-t/\tau_1)+\sum_{j=2}^{M}A_j\cos(\omega_j t+\alpha_j)\exp(-t/\tau_j). \qquad (19)$$

Here $\{A_j\}$ $(j=0,...,M)$ are the amplitudes, σ the temporal width of the Gaussian component, $\{\tau_j\}$ $(j=1,...,M)$ the relaxation times, $\{\omega_j\}$ $(j=2,...,M)$ the characteristic frequencies, and $\{\alpha_j\}$ $(j=2,...,M)$ their phases. The amplitudes $\{A_j\}$ are related by $\Delta R^*_b=-[A_0+A_1+\Sigma_{j=2}^{M}A_j\cos\alpha_j]$. Equation (19) contains contributions to the relaxation function from a short-time Gaussian, a longer time exponential expansion, and damped harmonic oscillations. The initial Gaussian time dependence is characteristic of short-time behavior of correlation functions.[51] The contribution of damped harmonic oscillations was first introduced by Uhlenbeck and Orenstein[57] and advanced by Kubo,[51] Robertson, and Yarwood,[39] Rothschild *et al.*,[40] and Mukamel and Fried[24–26] for the analysis of the response of condensed phases and clusters. Equation (19) was Fourier transformed, i.e., $F(\omega)=\mathrm{FT}_\omega\{F(t)\}$, to obtain

$$F(\omega)=(A_0/\sigma)(\pi/2)^{1/2}\exp\left(-\frac{\sigma\omega^2}{2}\right)+\sum_{j=1}^{M}\left[\frac{A_j/\tau_j}{(\omega-\omega_j)^2+(1/\tau_j)^2}+\frac{A_j/\tau_j}{(\omega+\omega_j)^2+(1/\tau_j)^2}\right], \qquad (20)$$

where $\omega_1=0$. Each peak in the FT, Eq. (20), was fit by a single Lorentzian to yield the amplitudes, frequencies $\{\omega_j\}$, and decay times $\{\tau_j\}$. These parameters were used as initial values for the subsequent fit of Eq. (19). Equation (19) was then fit by an iterative mean-least-square procedure to obtain the final amplitudes $\{A_j\}$, the temporal parameters σ and $\{\tau_j\}$, the frequencies $\{\omega_j\}$, and the phases $\{\alpha_j\}$. The fit of the simulated data by Eq. (19) is not unique and a somewhat different set of parameters (i.e., differences in 30%–40% in the values of the temporal parameters σ and $\{\tau_j\}$) also results in an adequate representation of the data. We have chosen the parameters with a minimal number of

TABLE I. Long-time structural parameters for Xe^*Ar_N clusters (averaged over a 1 ns trajectory). The corresponding data for the ground state $XeAr_N$ are given for comparison.

Type of cluster	T_i (K)[a]	$\langle T^* \rangle$ (K)	R_{NN} (Å)[b]	$\langle R^*_{NN} \rangle$ (Å)[c]	NN[b]	$\langle NN^* \rangle$[c]	R_{CM} (Å)[b]	$\langle R^*_{CM} \rangle$ (Å)[c]
Xe^*Ar_{146} (central)	10	26.5	3.72	4.54	12.0	17.5	0.083	3.98
Xe^*Ar_{146} (central)	30	36.4	3.77	4.48	12.0	12.1	0.17	2.49
Xe^*Ar_{146} (inner-1)	10	20.1	3.83	4.61	12.0	15.3	3.61	6.45
Xe^*Ar_{146} (inner-1)	30	35.6	3.89	4.63	12.0	14.9	3.67	5.69
Xe^*Ar_{146} (inner-2)	10	16.6	3.93	4.61	12.0	15.0	6.29	7.44
Xe^*Ar_{146} (inner-2)	30	34.7	3.99	4.69	12.1	11.6	6.37	8.20
Xe^*Ar_{146} (inner-3)	10	21.4	3.93	4.70	12.0	5.9	7.27	12.0
Xe^*Ar_{146} (inner-3)	30	37.5	3.99	4.74	12.0	5.2	7.35	12.3
Xe^*Ar_{146} (surf.-4)	10	14.9	4.03	4.63	9.0	8.0	9.01	10.4
Xe^*Ar_{146} (surf.-4)	30	32.6	4.07	4.66	8.9	7.7	9.09	10.5
Xe^*Ar_{146} (surf.-5)	10	13.2	4.04	4.65	8.0	7.9	9.77	10.9
Xe^*Ar_{146} (surf.-5)	30	32.0	4.08	4.70	7.8	6.8	9.86	11.0
Xe^*Ar_{146} (surf.-6)	10	12.3	4.07	4.67	6.0	5.9	11.1	12.0
Xe^*Ar_{146} (surf.-6)	30	31.3	4.11	4.73	5.8	4.2	11.2	12.4
Xe^*Ar_{147} (top)	10	12.1	4.04	4.65	3.0	3.2	12.0	12.6
Xe^*Ar_{147} (top)	30	33.1	4.08	4.73	2.9	3.1	12.1	12.9
Xe^*Ar_{54} (central)	10	41.4	3.79	4.70	12.0	4.7	0.11	8.56
Xe^*Ar_{54} (central)	30	41.7	4.09	4.79	14.0	4.7	1.40	8.53
Xe^*Ar_{54} (inner)	10	30.5	3.94	4.66	12.0	8.2	3.66	6.35
Xe^*Ar_{54} (inner)	30	36.7	4.02	4.77	12.1	4.4	3.71	8.27
Xe^*Ar_{54} (outer)	10	16.5	4.06	4.63	8.0	7.7	6.39	7.29
Xe^*Ar_{54} (outer)	30	35.9	4.10	4.72	7.7	2.7	6.40	9.47
Xe^*Ar_{54} (vertex)	10	14.7	4.08	4.68	6.0	5.9	7.35	8.17
Xe^*Ar_{54} (vertex)	30	35.6	4.12	4.70	5.8	4.8	7.46	8.37

[a]Initial cluster temperature.
[b]Structural parameters for the $XeAr_N$ clusters in the ground electronic state (Ref. 15).
[c]Asymptotic values for structural parameters for the Xe^*Ar_N clusters (see text).

frequencies in Eq. (19) to obtain an adequate fit (within $<1\%$) of the simulated data. The time dependence of the bubble configurational relaxation function in the short-time domain ($t \leqslant 1.5$ ps) is nearly independent of the initial cluster temperature (Fig. 1), while for longer times $F(t)$ at the higher temperature ($T_i = 30$ K) is smeared out and exhibits less details than at $T_i = 10$ K. The parameters $\{A_j\}$, σ, $\{\tau_j\}$, and $\{\omega_j\}$, obtained from the analysis of the $F(t)$ data for the bubble formation [sites (C) and (1)] in Xe^*Ar_{146}, are summarized in Table II. The good quality of the fit (Table II) is evident from Figs. 5 and 6. Within the uncertainty of the temporal parameters obtained from the fits, the site specificity and the temperature dependence of the lifetimes (Table II and Fig. 7) are weak.

(6) Bubble initial ultrafast time evolution. The short-time evolution is Gaussian (Figs. 1 and 5 and Table II), with the characteristic times $\tau_0 = 2^{1/2}\sigma$ in the range $\tau_0 \cong 170-280$ fs (Table II and Fig. 7). The initial Gaussian time evolution, which manifests the behavior of the relaxation function for the short-time radial expansion of the bubble, is pronounced (Fig. 5). This Gaussian form of the short-time evolution is manifested for all interior sites and also for surface sites. The site specificity (Fig. 7) and the temperature dependence of τ_0 are weak. The ultrafast time scale for the bubble initial expansion $\tau_0 = 170-180$ fs corresponds to effective vibrational frequencies of $1/c\tau_0 \cong 120-200\ \mathrm{cm}^{-1}$, which considerably exceed the characteristic nuclear vibrational frequencies of the rare-gas cluster (with a maximal vibrational frequency of $\sim 50\ \mathrm{cm}^{-1}$). Accordingly, the inertial radial bubble expansion, which corresponds to a Gaussian time evolution, occurs on a time scale faster than the cluster vibrational motion.

(7) Bubble exponential expansion. For the central site an exponential increase of the bubble size with a lifetime $\tau_1 = 2 \pm 0.5$ ps is exhibited with a rather weak temperature dependence of τ_1 (Fig. 8). This exponential component is not universal, e.g., not being exhibited by the interior (1) site (Table II).

(8) Characteristic bubble frequencies. For the (C) site two frequencies are exhibited (Table II), i.e., $\omega_2 \sim 7-9\ \mathrm{ps}^{-1}$ ($37-45\ \mathrm{cm}^{-1}$) and $\omega_3 \sim 3\ \mathrm{ps}^{-1}$ ($\sim 16\ \mathrm{cm}^{-1}$). There are two frequencies $\omega_3 \sim 16\ \mathrm{cm}^{-1}$ and $\omega_2 \sim 40\ \mathrm{cm}^{-1}$ which characterize bubble configurational relaxation in the interior sites (C), (1)–(3) of the Xe^*Ar_{146} cluster, with the ω_3 frequency being always exhibited, while the ω_2 frequency is less prominent (e.g., not appearing for site (1) at $T_i = 10$ K). The damping (dephasing) times of the two vibrational frequencies are $\tau_2 \cong 1-3$ ps (for ω_2) and $\tau_3 \cong 2-6$ ps (for ω_3), which are nearly temperature independent (Fig. 8). The vibrational frequencies ω_2 and ω_3 are in the range expected for the cluster frequencies. The characteristic times for the vibrational motion in the ω_2 and ω_3 modes, i.e., $1/c\omega_2 \cong 2$ ps and $1/c\omega_3 \sim 0.8$ ps, are comparable to or shorter than the dephasing times τ_2 and

TABLE II. Dynamic parameters for the characterization of the evolution of the structural mean guest-host distance $R^*_{NN}(t)$, the spectral shifts in emission $\delta\nu_e(t)$, and the cluster temperature $T^*(t)$ for Xe^*Ar_N ($N=146$ and 54) clusters at $T_i=10$ K. Each dynamic parameter $O(t)$ was represented in the form $O(t)=A_0\exp(-t^2/2\sigma^2)+A_1\exp(-t/\tau_1)+\Sigma_{j=2}^{L}A_j\exp(-t/\tau_j)\cos(\omega_j t+\alpha_j)$ with the corresponding relaxation function $F(t)=O(t)-\langle O\rangle$ being analyzed according to Eqs. (19) and (20).[a,b,c]

Observable			$R^*_{NN}(t)$				$\delta\nu_e(t)$				$T^*(t)$	
N	Site	j	τ_j (ps)	ω_j (ps^{-1})	A_j (Å)	α_j	τ_j (ps)	ω_j (ps^{-1})	A_j (eV)	α_j	τ_j (ps)	ω_j (ps^{-1})
146	(C)	0	0.17	-	−0.08	-	0.065	-	0.26	-	0.057	-
		1	1.8	0	−0.31	-	1.5	0	0.13	-	5	0
		2	2.1	8.5	−0.17	0.20	1.7	8.4	0.19	0.28	5	6.7
		3	6.1	3.3	−0.16	−0.33	3.9	3.3	0.17	−0.19	10	3.2
146	(I)	0	0.12	-	−0.43	-	0.12	-	0.48	-	0.064	-
		1	-	-	-	-	-	-	-	-	3	0
		2	-	-	-	-	0.5	7.7	0.11	−3.55	-	-
		3	1.4	3.3	−0.27	−1.50	2.7	3.6	0.07	−1.29	10	3.4
146	(4)	0	0.28	-	−0.36	-	0.14	-	0.20	-	0.081	-
		1	-	-	-	-	7.8	0	0.011	-	-	-
		2	2.5	6.7	−0.14	1.38	6.0	6.8	0.006	0.90	10	3.5
		3	4.1	3.3	−0.21	0.67	10.2	3.6	0.011	−0.8	7	4.8
146	(6)	0	0.21	-	−0.29	-	0.13	-	0.08	-	0.078	-
		1	-	-	-	-	0.55	0	0.057	-	-	-
		2	26	1.9	−0.20	−0.67	17.7	5.0	0.002	2.33	2	1.8
		3	-	-	-	-	19.8	2.0	0.012	−1.20	-	-
54	(C)	0	0.18	-	−1.19	-	0.11	-	0.35	-	0.059	-
		1	1.0	0	−0.60	-	1.3	0	0.12	-	-	-
		2	0.4	6.0	−1.45	2.66	1.2	6.7	0.06	1.59	2	3.5
		3	2.2	3.4	−0.39	0.27	2.0	3.5	0.15	−0.08	5	4.0
54	(I)	0	0.18	-	−0.24	-	0.12	-	0.32	-	0.085	-
		1	2.3	0	0.37	-	-	-	-	-	-	-
		2	0.9	3.1	−0.82	5.99	1.8	1.1	0.05	0.86	1	3.1
		3	1.8	5.2	−0.14	2.22	1.8	3.2	0.05	6.29	5	4.1
54	(O)	0	0.15	-	−0.16	-	0.15	-	0.097	-	0.085	-
		1	-	-	-	-	-	-	-	-	-	-
		2	2.5	1.3	−0.54	0.93	1.3	3.9	0.31	0.59	3	1.5
		3	4.0	2.8	−0.31	1.06	1.1	4.3	0.28	3.11	5	4.1
54	(V)	0	0.24	-	−0.88	-	0.12	-	0.10	-	0.081	-
		1	1.8	0	0.56	-	6.7	0	0.01	-	-	-
		2	4.1	17.4	−0.29	0.05	1.8	2.7	0.028	1.95	2	1.5
		3	40	2.1	−0.08	5.44	3.3	1.9	0.034	6.21	5	4.6

[a]Parameters for fit with a minimal number of frequencies to result in adequate (within 1%) representation of data.
[b]$\omega_1=0$ by definition.
[c]Entries in parentheses represent layer uncertainty (~50%).

τ_3. Within the uncertainty ($\pm 50\%$) of the data fit, frequencies [for interior sites (C), (1), and (2) of Xe^*Ar_{146}] exhibit a weak site specificity (Table II). The nuclear frequencies ω_2 and ω_3 reflect the dynamics of the motion of a nuclear wave packet accompanying the bubble formation induced by impact due to the switching on of the short-range repulsion in the electronically excited state.

(9) Other configurational changes. These involve the dislocation of the Xe* atom away from the cluster center of mass and the change in the number of nearest neighbors for the interior sites (C), (1), and (2). The configurational dilation is accompanied by the displacement of the Xe* atom in the bubble towards the exterior of the cluster as is evident from the time evolution of $R^*_{CM}(t)$ (Fig. 2 and Table I). Of particular interest is the dislocation of Xe* measured by

$$\delta R_{CM}=|\langle R^*_{CM}\rangle - R^*_{CM}(0)|. \tag{21}$$

For the central (C) site $\delta R_{CM}=2.3-3.9$ Å, for site (1) $\delta R_{CM}=2.0-2.8$ Å, and for site (2) $\delta R_{CM}=1.2-1.8$ Å (Table I). Concurrently, the coordination numbers for sites (C), (1) (Fig. 3 and Table I), and (2) markedly increase from their initial value $NN^*(0)=12$ to considerably larger values, e.g., $\langle NN^*\rangle=17-18$ for the (C) site and $\langle NN^*\rangle=15$ for site (1). Accordingly, the dislocation of Xe* is accompanied by a marked increase of the coordination number. A cursory examination of Figs. 2 and 3 reveals that the time scale τ_D for the exterior dislocation and for the change in the coordination number (specified by the time corresponding to the attainment of 90% of the asymptotic values) is $\tau_D\cong 4$ ps for the (C) site and $\tau_D\cong 1.5-2.0$ ps for sites (1) and (2) (at $T_i=10$ K). These values of τ_D are considerably longer than the (Gaussian) characteristic times [paragraph (a)(b)] for the bubble formation, i.e., $\tau_D \gg \tau_0$.

(10) Energy flow within the cluster. Relevant information was obtained from the time dependence of the cluster

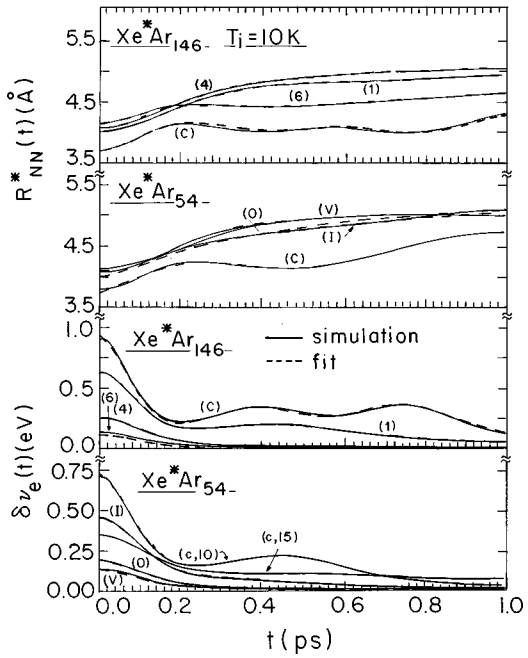

FIG. 5. Analysis of the short-time ($t=0-1$ ps) dynamics of the bubble formation and of the spectral shifts of Xe^*Ar_N ($N=54$ and 146) clusters. The time evolution of $R^*_{NN}(t)$, Eqs. (18) and (19) and of $\delta\nu_e(t)$, Eqs. (22) and (19), is fit with the parameters summarized in Table II. Solid lines represent the simulated curves while dashed curves represent the fit. Note the short-time Gaussian time evolution and the onset of impact induced vibrational coherence. The central (C), internal (I), and surface (4) and (6) sites for $N=146$ and central (C), internal (I), and surface (O) and (V) sites for $N=54$ are marked on the curves. All data are for $T_i=10$ K, except for the (C) site of $N=54$, which is given for $T_i=10$ K (marked C10) and for $T_i=15$ K (marked C15 and not fit). Note that the ground-state dislocation of Xe in $XeAr_{54}$ at $T_i=15$ K results in the reduction of $\delta\nu_e(0)$ relative to its value at $T_i=10$ K.

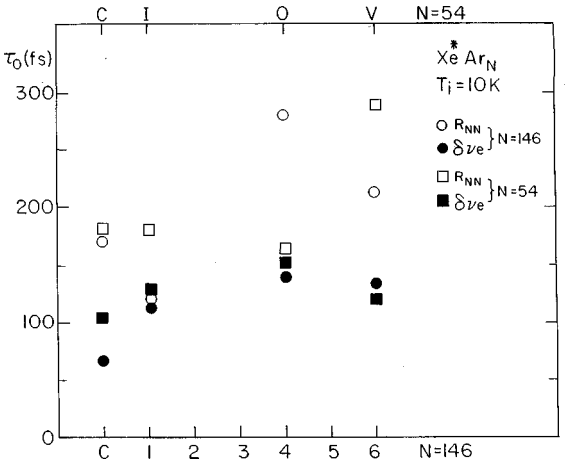

FIG. 7. Site specificity of the initial Gaussian characteristic time τ_0 for the structural dynamics of $R^*_{NN}(t)$ and for the spectroscopic dynamics of $\delta\nu_e(t)$ for Xe^*Ar_N ($N=54$, 146) clusters at $T_i=10$ K. The lower horizontal scale marks the sites for the $N=146$ cluster (with data denoted by circles), while the upper horizontal scale marks the sites for the $N=54$ cluster (with data denoted by squares).

kinetic energy expressed by the temperature $T^*(t)$, Eq. (3). The long-time $\langle T^*\rangle$ cluster temperatures (averaged over 1 ns) are summarized in Table I. The temperature rise $\Delta T=\langle T^*\rangle - T_i$ for the interior states is quite substantial, i.e., $\Delta T\approx 16$ K for $T_i=10$ K and $\Delta T\approx 4-6$ K for $T_i=30$ K. At $T_i=10$ K site specificity of ΔT is exhibited, with $\Delta T(\mathrm{C})>\Delta T(1)>\Delta T(2)$.

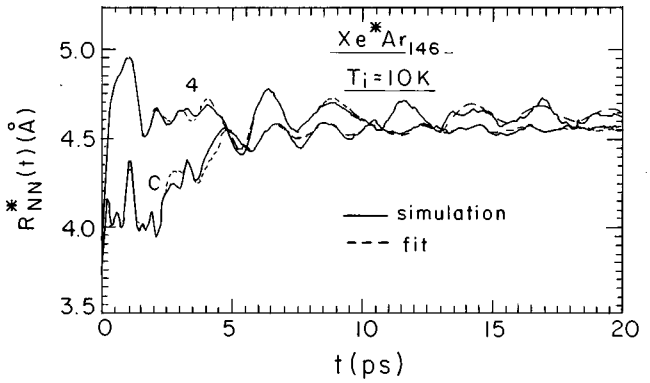

FIG. 6. Analysis of the structural dynamics of the bubble formation for site (C) and for the spring formation for site (4) in Xe^*Ar_{146} clusters at $T_i=10$ K. Solid curves represent the simulated data while dashed curves represent the fits with the parameters summarized in Table II.

The time evolution of $T^*(t)$ (Fig. 4) for the interior (C), (1), and (2) sites exhibits a fast increase, a slower exponential, and a marked oscillatory dependence. The temperature relaxation function $F_T(t)=|T^*(t)-\langle T^*\rangle|$ was analyzed in an analogous manner to Eqs. (18)–(20), with the characteristic times and frequencies being summarized in Table II. The initial increase of $T^*(t)$ is Gaussian, with a characteristic time $\tau_{ET}=2^{1/2}\sigma\cong 50-60$ fs. Accordingly, $\tau_{ET}<\tau_0$, reflecting ultrafast energy transfer into the cluster, which triggers the bubble expansion process. The ultrafast time scale for energy flow into the cluster $\tau_{ET}=50-60$ fs corresponds to an effective vibrational frequency $1/c\tau_{ET}\sim 600\ \mathrm{cm}^{-1}$, which considerably exceeds all the characteristic frequencies of the cluster

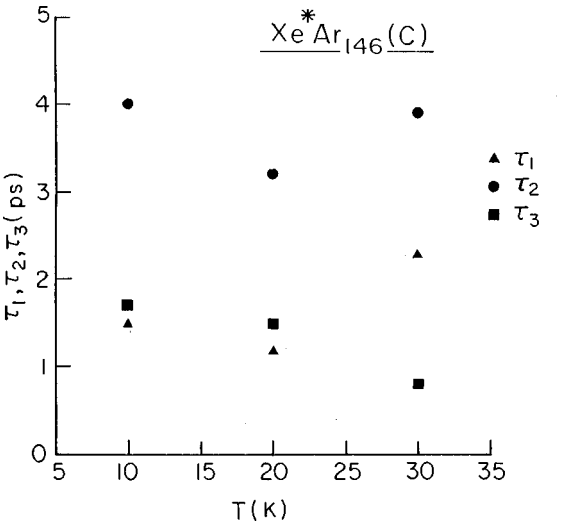

FIG. 8. The temperature dependence of the exponential decay time τ_1 and the damping times τ_2 and τ_3 of the vibrational coherence for the (C) site of Xe^*Ar_{146}.

(upper limit of $\sim 50\ cm^{-1}$). Accordingly, the cluster is frozen on the time scale of the initial energy flow, which is equivalent to the impact-induced excitation. Subsequently, a slower exponential increase of $T(t)$ occurs with $\tau_1 \cong 3-5$ ps (Table II). This is followed by an oscillatory behavior of $T(t)$, e.g., for the (C) site the oscillation frequencies are $\sim 3\ ps^{-1}$ ($\sim 16\ cm^{-1}$), and $\sim 7\ ps^{-1}$ ($\sim 37\ cm^{-1}$), reflecting the exchange between the kinetic energy and the potential energy in the cluster. The characteristic $T^*(t)$ oscillation frequencies ($16\ cm^{-1}$ and $37\ cm^{-1}$) are similar to the frequencies of the configurational relaxation of the bubble (Table II).

(11) A structural criterion for interior sites of Xe*. A structural specification of the surface Xe substitutional sites can be obtained from the ground state equilibrium values of $R_{CM}(0)$, which are: 9.0 Å for site (4), 9.8 Å for site (5), and 11.2 Å for site (6) (Table I). Accordingly, Xe* remains in the interior of the cluster when $\langle R_{CM}\rangle \leqslant 9.0$ Å. This condition is satisfied for sites (C), (1), and (2), whose temporal and asymptotic structural parameters indeed show that they remained inside the cluster during the entire bubble relaxation process.

(12) The intermediate case of site (3). The asymptotic parameter $\langle R_{CM}\rangle = 12.0-12.3$ Å for the Xe^*Ar_N cluster initially substituted in the interior site (3) (Table I) is $\langle R_{CM}\rangle > 9.0$ Å, violating the condition for the location of Xe* in an interior cluster site (see preceding paragraph). The Xe* atom initially located in interior site (3) was liberated from the interior and occupies a surface site. This is evident from the drastic reduction of the coordination number for this site from $NN^*(0) = 12$ to $\langle NN^*\rangle = 5-6$, which indeed corresponds to the Xe* surface site (Table II and Fig. 3). We are thus facing a dynamic dislocation from the interior to the surface substitutional site, driven by electronic extravalence excitation. This brings us to the structural dynamics of surface excitations.

(b) *The spring formation for extravalence excitations in the surface sites (4), (5), (6), and (T).*

(1) Stretching and contraction of $R^*_{NN}(t)$. Following vertical excitation $R^*_{NN}(t)$ increases up to its highest $R^*_{NN}(\tau_M)$ value, at $t=\tau_M$, assuming the values of $R^*_{NN}(\tau_M) = 4.92$, 5.00, 5.25, and 5.10 Å for sites (4), (5), (6), and (T), respectively (Fig. 1). The characteristic time for the attainment of $R^*_{NN}(\tau_M)$ is $\tau_M = 1.3$ ps for sites (4) and (5) and $\tau_M \cong 2.0$ ps for sites (6) and (T). These values of $R^*_{NN}(\tau_M)$ are only slightly lower than the upper limit $1.15\ r_e = 5.35$ Å for the nearest-neighbor distance (Sec. II B). $R^*_{NN}(\tau_M)$ exceeds the asymptotic $\langle R^*_{NN}\rangle$ value for all surface sites (Table I and Fig. 1), with the relative increase, Eq. (17), of $R^*_{NN}(\tau_M)$ being $f(\tau_M) \cong 1.5-2.0$. Subsequently, for $t > \tau_M$ an oscillatory nuclear relaxation to the asymptotic $\langle R^*_{NN}\rangle$ value is exhibited (Fig. 1).

(2) Average long-time displacements. The $\Delta R^*_{NN} = \langle R^*_{NN}\rangle - R^*_{NN}(0)$ values are $\Delta R^*_{NN} = 0.61$ Å for sites (4), (5), and (6) and $\Delta R^*_{NN} = 0.65$ Å for the (T) atom. These values of R^*_{NN} are nearly surface-site independent.

(3) Multimodal time evolution of $R^*_{NN}(t)$ from its initial value $R^*_{NN}(0)$ to the asymptotic value $\langle R^*_{NN}\rangle$. The time evolution exhibits short-time Gaussian behavior followed by an oscillatory one, which manifests the vibrational motion of the Xe* atom with respect to the cluster (Fig. 1 and Table II).

(4) Spring relaxation dynamics. The analysis of the configurational change was performed by defining the configurational relaxation function $F(t)$, Eq. (18), for sites (4)–(6) and (T), and carrying out the analysis according to Eqs. (19) and (20). Typical parameters $\{A_j\}$, $\tau_0 = 2^{1/2}\sigma$, $\{\tau_j\}$, $\{\omega_j\}$, and $\{\alpha_j\}$ are summarized in Table II. The initial times for structural relaxation are $\tau_0 = 200-300$ fs, which are not surface site specific. The τ_0 values for the spring dynamics in the surface sites (4)–(6) may be somewhat longer than the corresponding $\tau_0 = 170-280$ fs lifetimes for the bubble formation [see paragraph (a)(6) of this Sec.], but their difference lies within the data fit uncertainty. As for the bubble formation [paragraph (a)(6)], the characteristic frequencies $1/c\tau_0 \sim 110-160\ cm^{-1}$, characterizing the inertial radial spring motion, exceed the cluster vibrational frequencies. The initial ultrafast spring stretching is followed by longer-time (ps) oscillatory behavior with several modes with the characteristic lifetimes in the range $\cong 2-20$ ps. The number of oscillatory components decreases and the characteristic time lengthens from site (4) to (6), i.e., with the initial displacement of Xe* from the cluster center (Table II).

(5) Spring frequencies. The characteristic frequencies for Xe* spring motion fall in the range $\sim 2-4\ ps^{-1}$ ($11-22\ cm^{-1}$) (Table II). For site (4) the two spring frequencies of $\sim 3\ ps^{-1}$ ($16\ cm^{-1}$) and $\sim 7\ ps^{-1}$ ($38\ cm^{-1}$) are close to those of the bubble [paragraph (a)(8)]. On the other hand, for the exterior surface site (6) the characteristic frequency is reduced to $2\ ps^{-1}$ ($\sim 11\ cm^{-1}$). For the motion of the exterior surface site (6) a long-time, low frequency motion with $\tau_2 \cong 20$ ps is exhibited (Fig. 6 and Table II). The frequencies ω_2 and ω_3 fall in the range expected for the cluster frequencies. The characteristic times for the ω_2 and ω_3 vibrational modes, e.g., $1/c\omega_j = 1-2$ ps ($j=2,3$), are shorter than the damping lifetimes τ_2 and τ_3.

(6) Dislocation of Xe* outside the cluster. This can be inferred from the behavior of $R^*_{CM}(t)$ (Fig. 2). The increase of $R^*_{NN}(t)$ (Fig. 1) is accompanied by an increase of $R^*_{CM}(t)$ (Fig. 2). The dislocation of Xe*, δR_{CM}, Eq. (21), assumes the values (Table I) 1.4, 1.1, 0.8–1.2, and 0.7–0.8 Å for sites (4), (5), (6), and (T), respectively. These values of δR_{CM} exhibit a decrease of the stretching for more distant sites. The time scale τ_D for the increase of R^*_{CM} [paragraph (a)(9)] is $\tau_D \cong 1.5$ ps (Fig. 2), being site independent for the surface

sites. The τ_D values for the surface sites are considerably lower than the corresponding $\tau_D \cong 4$ ps value for the bubble in the (C) site (Fig. 2). Again, $\tau_D > \tau_0$, with the time scale for Xe* dislocation being considerably longer than the initial spring configurational relaxation. On the other hand, $\tau_D \cong \tau_M$, with the time scale for the attainment of the maximum value of the stretching [i.e., of $R^*_{NN}(t)$] approximately coinciding with the Xe* dislocation time, as expected. The asymptotic value of $\langle R^*_{CM} \rangle = 12.0-12.4$ Å for site (6) is equal to or exceeds the initial value of $R_{CM} = 12.0$ Å for site (T) (Table I). Accordingly Xe*, initially in a surface state (T), relaxes to a configuration outside the ground state cluster.

(7) Coordination numbers. An oscillatory temporal behavior of NN*(t) is exhibited (Fig. 3). The initial decrease of NN*(t) at short times clearly manifests the spring stretching with the dislocation of Xe* away from the cluster. The asymptotic values of $\langle$NN*$\rangle$ for the surface sites are close to those of the initial NN*(0)=NN values (Table I).

(8) Lack of dissociation of Xe*. The finite, constant asymptotic values of $\langle R^*_{CM} \rangle$ and of $\langle$NN*$\rangle \cong$NN for the Xe* surface sites (Figs. 2 and 3 and Table I) clearly imply that the surface Xe* atoms in sites (4)–(6) and (T) remain bound.

(9) Energy flow to the cluster. The time evolution of the cluster temperature for surface sites (4)–(6) and (T) (Fig. 4) is characterized by the ultrafast rise (Table II) of $\tau_{ET} \cong 80$ fs. τ_{ET} is shorter than $\tau_0 \cong 200-300$ fs [paragraph (b)(4)] and reflects ultrafast energy flow into the cluster, which triggers the configurational change. The time scale τ_{ET} for the spring is again, as for the bubble [paragraph (a)(10)], considerably shorter than the time scale for the cluster vibrational motion, with the cluster being frozen on the time scale of the initial impact energy transfer. The subsequent oscillatory behavior of $T(t)$ (Fig. 4) manifests the exchange between kinetic and potential energy. The frequencies of this energy exchange (Table II) $\omega \sim 3-5\ (\text{ps})^{-1}$ for site (4) and $\omega \sim 2\ (\text{ps})^{-1}$ for the exterior site (6) are close to the frequencies accompanying the configurational change (Table II).

(10) The initial temperature dependence of the temporal and asymptotic structural parameters. For the initial cluster temperatures of $T_i = 10$ K and 30 K the structural and dynamic parameters exhibit a weak temperature dependence, and do not exhibit any systematic variation exceeding the uncertainty of our analysis.

This concludes our analysis of the dynamics of bubble formation around internal Xe* sites and spring formation for surface Xe* sites. Three final points should be made.

(1) Universal features of the dynamics of large Xe^*Ar_N clusters were established. Similar temporal and asymptotic structural attributes were obtained for $N = 146$ reported herein, and for larger $N = 199$ clusters.

(2) The large Xe^*Ar_{146} cluster preserves its integrity during the configurational relaxation processes. On the longest time scale of 1 ns used in our simulations, no dissociation of the cluster was exhibited. All the nuclear relaxation processes are nondissociative, being reminiscent of vibrational energy flow and vibrational relaxation in the condensed phase.

(3) No rigid–nonrigid cluster structural transition was induced for ''large'' clusters. The large Xe^*Ar_{146} cluster also remains rigid during the dynamic processes initiated at the initial temperature $T_i \leqslant 30$ K and no cluster ''melting'' is exhibited.

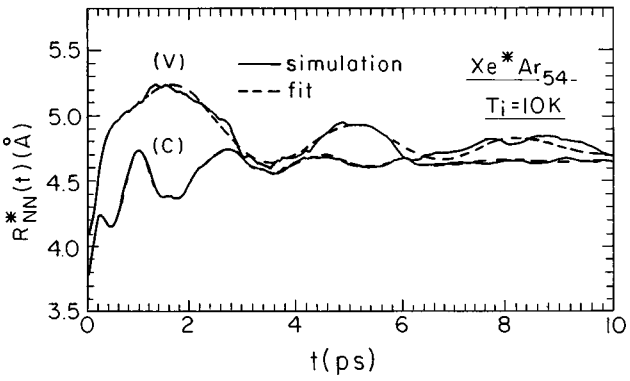

FIG. 9. Site-specific time dependence of the structural parameter $R^*_{NN}(t)$ for the central (C) and the surface (V) Xe site in Xe^*Ar_{54} clusters at $T_i = 10$ K. The solid lines represent the simulation results. The dashed line represents the fits, Eqs. (18) and (19), with the parameters given in Table II.

IV. STRUCTURAL RELAXATION IN Xe^*Ar_{54} CLUSTERS

With decreasing the cluster size a new type of structural relaxation phenomenon is expected on the basis of previous simulations for $Xe_2^*Ar_{53}$ clusters.[22] In intermediate size Xe^*Ar_{54} clusters, the excessive vibrational energy flow to the cluster may induce rigid–nonrigid (melting) transition within the cluster. Our simulations reveal that vertical excitation of the $XeAr_{54}$ cluster (at $T_i = 10$ K), with the Xe atom initially located at the cluster center, results in a nonrigid Xe^*Ar_{54} cluster, where diffusion of the Xe* atom from the interior site to the surface occurs. Concurrently, this intermediate size Xe^*Ar_{54} cluster maintains its integrity and dissociative processes are negligible, i.e., not exceeding the dissociation of a single Ar atom on the relevant (~ 1 ns) time scale.

The time evolution of the structural parameters R^*_{NN} (Fig. 9), R^*_{CM} (Fig. 10), and the cluster temperature $T^*(t)$ (Fig. 11) of Xe^*Ar_{54} was explored for the four Xe* substitutional sites,[15] i.e., (C) center, (I) interior, (O) and (V) surface sites. The asymptotic data were summarized in Table I. The analysis of the cluster temperature (Fig. 11) $F_T(t) = T^*(t) - \langle T \rangle$, according to Eqs. (19) and (20), results in the temporal and frequency parameters summarized in Table II. The ultrafast Gaussian time evolution for initial energy flow into the cluster is characterized by a time $\tau_{ET} = 2^{1/2}\sigma$, i.e., $\tau_{ET} = 60$ fs for the central site (C) and $\tau_{ET} \sim 80$ fs for the interior site (I) and for the surface sites (O) and (V). The time

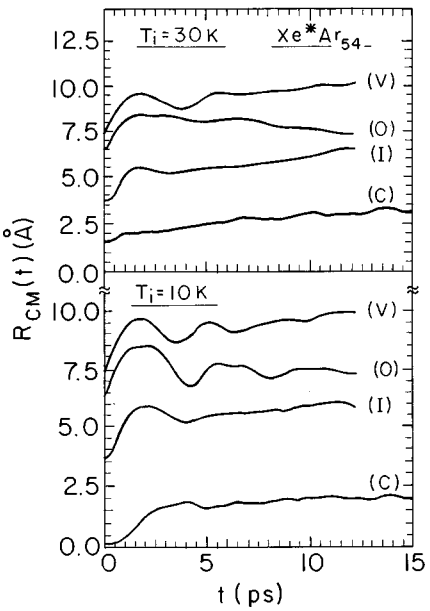

FIG. 10. The site-specific time dependence of the distance $R_{CM}(t)$ between Xe* and the center of mass of the cluster for different Xe* substitutional sites (marked on the curves) at initial temperatures $T_i=10$ K and $T_i=30$ K (marked on the panels). Note the initial dislocation $[R_{CM}(0)=1.6\text{Å}]$ of the central (C) Xe atom at $T=30$ K.

evolution of $R^*_{NN}(t)$ (Fig. 9) exhibits an initial Gaussian increase followed by damped oscillatory components. The analysis of $F(t)$, Eq. (18), was performed using Eqs. (19) and (20). The relaxation parameters at $T_i=10$ K, summarized in Table II, result in a good fit (Figs. 5 and 9). The energy transfer and relaxation parameters $\tau_{ET},\tau_0,\tau_1-\tau_3,\omega_2,\omega_3$ for the interior (C) and (I) and for the surface (O) and (V) sites of Xe^*Ar_{54} (Table II) are similar to those of the interior and surface sites of Xe^*Ar_{146} (Sec. III), so that no marked cluster size dependence of the configurational bubble and spring relaxation is exhibited in this cluster size domain. For the interior sites (C) and (I) the initial Gaussian decay time is $\tau_0\cong 180$ fs, which is longer than τ_{ET}, followed by an exponential decay with $\tau_1\cong 1$ ps for the (C) site and $\tau_1\cong 2$ ps for the (I) site. Vibrational coherence for sites (C)

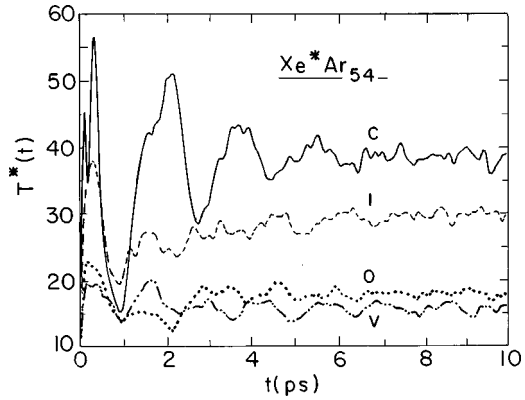

FIG. 11. The time evolution of the cluster temperature $T^*(t)$ for the Xe^*Ar_{54} cluster for different Xe* substitutional sites (marked on the curves) for the initial temperature $T_i=10$ K.

and (I) is characterized by two frequencies: $\omega_2\cong 5$–$6\ (\text{ps})^{-1}$ and $\omega_3\cong 3\ (\text{ps})^{-1}$. The interior Xe excitations at sites (C) and (I), which are accompanied by a large configurational dilation (Fig. 9) of $\langle R^*_{NN}\rangle - R_{NN}=0.8$–$0.9$ Å, correspond to the bubble formation. The structural parameters $R^*_{CM}(t)$ for the (C) and (I) sites of Xe^*Ar_{54} at $T_i=10$ K exhibit an initial increase on the time scale of $\tau_D=2.5$ ps for (C) and $\tau_D=1.5$–2.0 ps for (I) (Fig. 10), which considerably exceeds τ_0 and manifests the dislocation of Xe*. It is also instructive to note that for the (C) site at $T_i=30$ K, a thermally induced, site-specific, configurational change with $R^*_{CM}(0)=1.4$ Å is exhibited [in contrast to $R^*_{CM}(0)=0.1$ at $T_i=10$ K] and a further dislocation of Xe* occurs from $R_{CM}(0)=1.4$ Å to $R^*_{CM}(t=10\text{ ps})\cong 2.4$ Å (Fig. 10). For both the (C) and (I) sites at $T_i=10$ K and at $T_i=30$ K the Xe* atom remains inside the cluster on a time scale of ~ 10 ps with R^*_{CM} $(t=10$ ps) for these sites being smaller than the corresponding initial R_{CM} value for the surface sites (O) or (V) (Table I). For longer time scales of 50–1000 ps further cluster configurational changes are exhibited, resulting in the increase of $R^*_{CM}(t)$ on this time scale and of $\langle R^*_{CM}\rangle$ (Table I), which will be subsequently discussed. The Xe^*Ar_{54} surface state (V) exhibits spring formation, with a marked increase of $R^*_{CM}(t)$ beyond the ground-state cluster boundary (Fig. 10 and Table I) and with a marked decrease of the coordination number $\langle NN^*\rangle$ (Table I). Vibrational coherence effects for the surface site (V) exhibit a frequency of $2\ (\text{ps})^{-1}$ $(11\ \text{cm}^{-1})$ with a long lifetime (Fig. 11 and Table II), which characterizes the spring motion. The short-time configurational site-specific dynamics (on a time scale of ~ 20 ps) of Xe^*Ar_{54} is quantitatively similar to that of Xe^*Ar_{146}.

The long-time (1 ns) behavior of Xe^*Ar_{54} reflects new implications of cluster melting. The final temperature of the Xe^*Ar_{54} cluster in the initial (C) Xe* site is $\langle T^*\rangle=42$ K (Fig. 12), this limiting temperature (independent of T_i) is reached after $t=10$ ps (Fig. 11). As the melting temperature of Ar_{55} is $T_M=30$ K,[58,59] we expect that for $XeAr_{54}$ at $\langle T\rangle=42$ K a cluster total rigid–nonrigid transition (melting) has occurred. Very large configurational changes of the Xe* microenvironment are exhibited on a time scale of 200 ps, with R^*_{CM} increasing from the initial values of $R^*_{CM}(0)=0.5$ Å at $T_i=10$ K and $R^*_{CM}(0)=2$ Å at $T_i=30$ K to a larger finite value $R^*_{CM}(t>250\text{ ps})=8.5$ Å (Fig. 12), resulting in the large value of $\langle R^*_{CM}\rangle=8.5$ Å (averaged over 1 ns) which is given in Table I. Concurrently, the number of Xe* nearest neighbors decreases from $NN^*(0)=12$–14 to the low value $NN^*(t>250\text{ ps})=5$ (Fig. 12 and Table I). Such long-time configurational changes, characteristic of the medium-sized Xe^*Ar_{54} cluster (Fig. 12), are not exhibited in a large, e.g., Xe^*Ar_{199}, cluster (Fig. 13). These dramatic long-time configurational changes in Xe^*Ar_{54} (Fig. 12) manifest mass transport of the Xe* atom from the central site to the surface of the nonrigid cluster. A crude representation of the Xe*–Ar pair potential in terms of the LJ potential, i.e., $\epsilon=8\times 10^{-3}$ eV and $\sigma=4.13$ Å,[15–17] which, according to the recipe of Perera and Amar,[49] corresponds to the reduced parameters $\sigma^*=1.213$ and $\epsilon^*=0.77$. For a low value of ϵ^* the

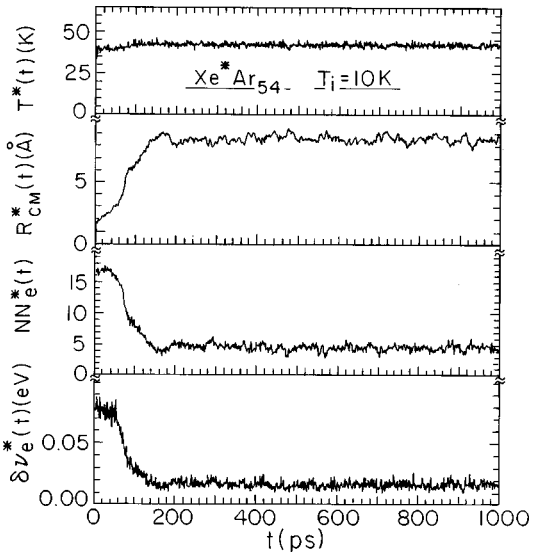

FIG. 12. The long-time ($t=0-1$ ns) behavior of the temperature $T^*(t)$, the structural parameters $R^*_{CM}(t)$ and NN*(t), and the time-dependent emission spectral shift $\delta\nu_e(t)$ of the Xe^*Ar_{54} cluster, where the Xe* atom was initially located at the central (C) site at $T_i=10$ K. The break in the structural parameters and in $\delta\nu_e(t)$, which saturate at ~ 200 ps, marks the diffusion of the Xe* bubble to the cluster surface.

surface site is expected to be preferred.[49] Indeed, the Xe* does prefer the surface site, as borne out by our simulations (Fig. 12). During the mass transfer to the surface R^*_{NN} is almost not changed, i.e., the Xe* atom drags along its bubble. The time scale for the mass transfer of Xe* from the center to the surface is ~ 150 ps at $\langle T^*\rangle = 42$ K. In conclusion, in the Xe^*Ar_{54} cluster the local short-time (10 ps) configurational change of bubble formation is followed by a global long-time (150 ps) configurational change, which involves Xe* transport to the surface.

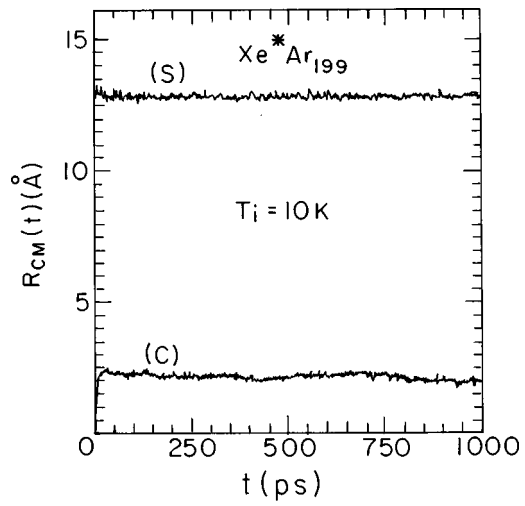

FIG. 13. The long-time ($t=0-1$ ns) dependence of $R^*_{CM}(t)$ for the central (C) and surface (S) sites (marked on the curves) of Xe^*Ar_{199} excited at $T_i=10$ K. The time independence of $R_{CM}(t)$ reflects cluster rigidity.

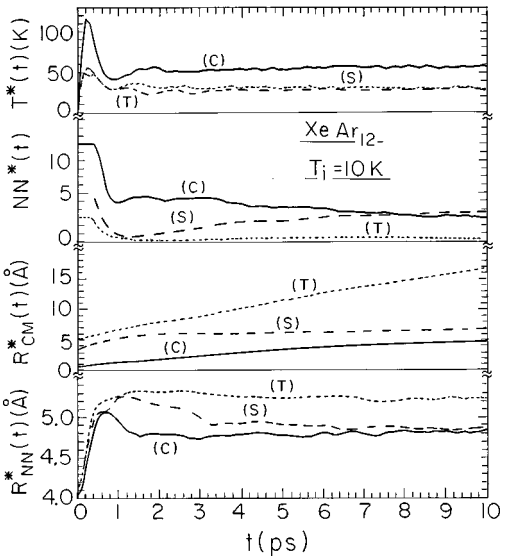

FIG. 14. The site-specific time dependence of the cluster temperature $T^*(t)$ and the structural parameters $R^*_{NN}(t)$, $R_{CM}(t)$, and NN*(t) for the central (C) and surface (S) sites for Xe^*Ar_{12} and the top (T) site of Xe^*Ar_{13} (marked on the curves). Clusters excited at $T_i=10$ K.

V. DISSOCIATIVE DYNAMICS IN SMALL Xe^*Ar_{12} CLUSTERS

For large ($N=146,199$) and medium-sized ($N=54$) clusters the dynamics is essentially ''nonreactive'' with the cluster maintaining its structural integrity on the relevant (ns) time scale. For a small cluster, i.e., Xe^*Ar_{12}, the vibrational energy flow results in dissociative cluster dynamics. We have studied energy acquisition, configurational relaxation, and dissociation for small Xe^*Ar_{12} clusters, exploring the initial central (C), surface (S), and top (T) Xe* atom configurations. The initial vibrational energy flow into the cluster, following the electronic excitation (at $T_i=10$ K) as inferred from the time evolution of the cluster temperature (Fig. 14) $\tau_{ET}\cong 100$ fs for the (C), (S), and (T) sites, is independent of the initial site. $T^*(t)$ subsequently reaches a peak value specified by T^*_{MAX} with the temperature rise $\Delta T = T^*_{MAX}-T_i$, i.e., $\Delta T=110$ K at $t\cong 250$ fs for the (C) site and $\Delta T\cong 45-50$ K for the (S) and (T) sites at $t\cong 200$ fs (Fig. 14). The very large value of ΔT for the (C) site considerably exceeds the cluster melting temperature[58,59] and leads to a substantial disintegration of the cluster.

The products of the cluster dissociation can be represented in terms of the time dependent fraction $P(N)$ of N-body clusters. The average number N of atoms in the cluster can be written as $N=\Sigma_N NP(N)$. The yields $Y(N)=(N/N)P(N)$ of N-body clusters are subjected to the normalization condition $\Sigma_N Y(N)=1$, for each t. Figure 15 portrays the time dependence of the fractions $P(N)$ of N-body clusters from Xe^*A_{12} at $T_i=10$ K (obtained by the averaging over 100 trajectories). The Xe^*Ar_{12} cluster disintegration is site specific. The most extensive fragmentation occurs for the (C) site, while the (S) and (T) sites reveal only a small amount $[P(1)\leqslant 0.25]$ of single atom dissociation on the time scale of 10 ps (Fig. 15). An incubation time τ_{IN} for

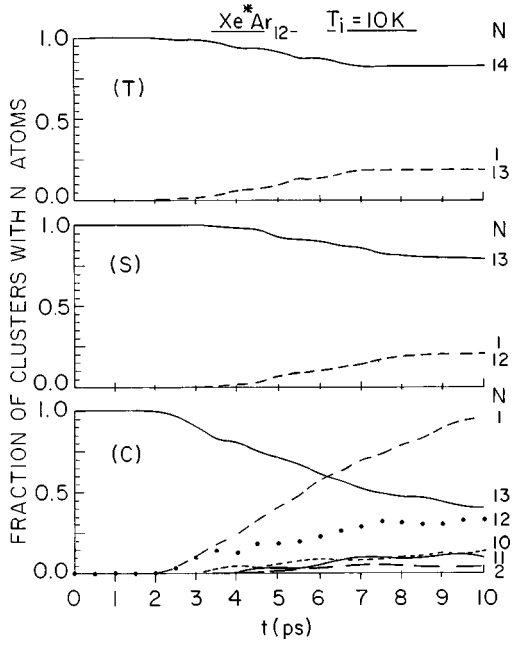

FIG. 15. The time dependence of the fractions P(N) of N-atom clusters in the fragmentation of Xe^*Ar_{12} [central (C) and surface (S) Xe* sites] and of Xe^*Ar_{13} [top (T) Xe* site]. The sites are marked on the panels. Initial temperature $T_i = 10$ K.

dissociation is exhibited, i.e., $\tau_{IN} \cong 2$ ps for the (C) site and $\tau_{IN} \cong 3.5$ ps for the (S) and (T) sites. These incubation times considerably exceed τ_{ET}, as well as the characteristic times τ_0 for the initial configurational changes (Fig. 14) of R^*_{NN} ($\tau_0 \sim 200$–300 fs) and of NN* (characteristic times ~ 800 fs). The major dissociation route of Xe^*Ar_{12} at the (C) site involves single atom sequential dissociation. At 10 ps, 60% of the Xe^*Ar_{12} (C) clusters disintegrated, mostly via the ''evaporation'' of a single atom [where $P(1) \cong 0.95$ at $t = 10$ ps], while the fraction of dimers is small (i.e., $P(2) < 0.05$) (Fig. 15). From the structural data of Fig. 14 it appears that the average number of the first nearest neighbors is NN*$\sim$4 and the average distance is $R^*_{NN} = 4.6$ Å for the (C) and (S) sites at $t = 10$ ps. Thus the Xe* atom initially located at the (C) and (S) sites of Xe^*Ar_{12} does not leave the residual cluster on the time scale of 10 ps. On the other hand, the low value of NN*<1 at $t = 10$ ps for the $Ar_{13}Xe^*$ (T) cluster (Fig. 14) reveals that Xe* dissociation took place from the (T) site. In conclusion, the dissociative dynamics of small Xe^*Ar_{12} and Xe^*Ar_{13} heteroclusters is site specific, involving mainly consecutive single atom dissociation events.

This dissociative dynamics of small clusters is not induced by vibrational energy transfer from a guest diatomic molecule[60] or an excimer molecule[22] to the cluster, which was previously explored,[22,60] but rather from the induced short-range guest Rydberg-host atoms repulsion. Regarding dynamic cluster size effects the dynamics of these impact excited small clusters marks the limit of dissociative molecular-type dynamics, while with increasing the cluster size (Secs. III and IV) a ''transition'' from the small-cluster molecular-type dynamics to the large-cluster repulsive induced configurational dynamics in an elemental atomic cluster is exhibited.

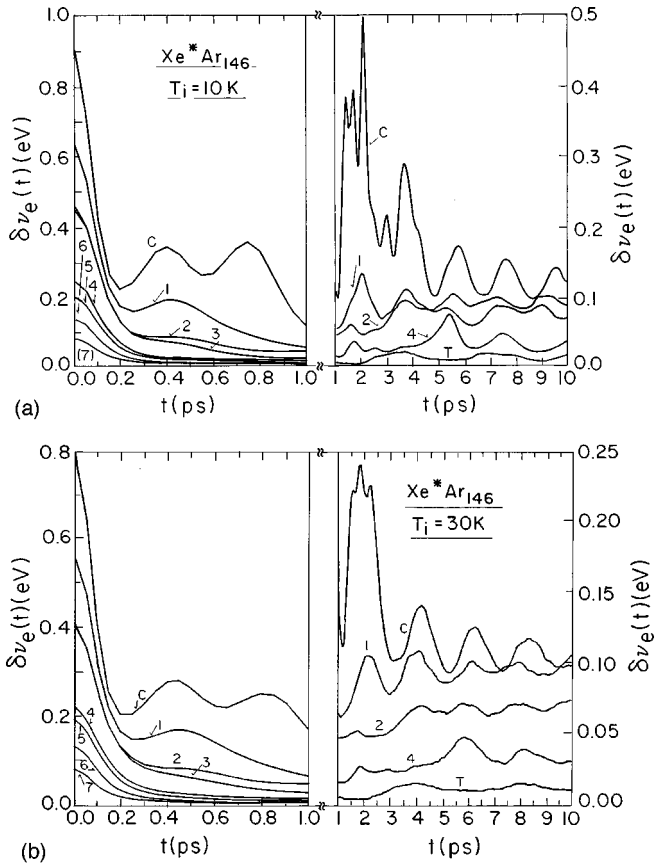

FIG. 16. The time dependence of the site-specific spectral shifts in emission for Xe^*Ar_{146} clusters. The Xe* substitutional sites are marked on the curves. (a) $T_i = 10$ K. (b) $T_i = 30$ K.

VI. TIME DEPENDENT SPECTRAL SHIFTS IN EMISSION

We proceed to explore the experimental spectroscopic implications of large configurational relaxation in large ($N = 146$) and medium-sized ($N = 54$) Xe^*Ar_N clusters. The time-resolved spectral shifts in emission [Figs. 16(a) and 16(b)] reveal a marked time-dependent evolution towards lower $\delta\nu_e$ values, which provide the spectroscopic manifestation of the configurational changes, i.e., the bubble formation for interior Xe* sites and the spring effect for Xe* surface sites. Of course, the configurational dilation, which increases the Xe*–Ar distances both for interior and surface Xe* sites, will result in the marked time dependent reduction of the (blue) spectral shift in emission from the large value $\delta\nu_e(0) = \delta\nu$ to considerably lower values. The asymptotic values of $\langle \delta\nu_e \rangle$ of the emission spectral shifts, together with the large asymptotic Stokes shifts (each averaged over 10 trajectories of 1 ns), are summarized in Table III. The time-resolved spectral shifts $\delta\nu_e(t)$ in emission [Figs. 16(a) and 16(b)] were characterized by the spectral shift relaxation function

TABLE III. Characterization of the energetics of the emission spectra of Xe^*Ar_{146} clusters (after $t=1$ ns). The spectral shifts $\delta\nu$ and linewidths Γ for absorption are also given.

Xe* site[a]	T_i (K)[b,c]	$\langle\delta\nu_e\rangle$ (eV)[d]	$\delta\nu$ (eV)[e]	$\langle SS\rangle$ (eV)[f]	Γ_e (eV)[d]	Γ (eV)[e]
Central	10	0.102	0.92	0.82	0.062	0.084
Central	30	0.087	0.80	0.71	0.090	0.14
Inner-1	10	0.097	0.63	0.54	0.053	0.073
Inner-1	30	0.092	0.55	0.46	0.044	0.13
Inner-2	10	0.078	0.46	0.38	0.035	0.073
Inner-2	30	0.059	0.41	0.35	0.045	0.12
Inner-3	10	0.022	0.45	0.43	0.033	0.073
Inner-3	30	0.025	0.40	0.37	0.036	0.12
Surface-4	10	0.036	0.25	0.21	0.023	0.059
Surface-4	30	0.033	0.23	0.20	0.031	0.10
Surface-5	10	0.032	0.21	0.18	0.018	0.056
Surface-5	30	0.028	0.20	0.17	0.025	0.094
Surface-6	10	0.021	0.14	0.12	0.014	0.051
Surface-6	30	0.018	0.013	0.12	0.020	0.082
Top	10	0.013	0.083	0.070	0.021	0.038
Top	30	0.011	0.079	0.068	0.022	0.064

[a]Labeling of sites.
[b]Initial ground state temperature.
[c]Final excited state temperature given in Table I.
[d]Spectral parameters for emission for Xe^*Ar_N. $\langle\delta\nu_e\rangle$-spectral shift and Γ_e-linewidth.
[e]Spectral parameters for absorption for $XeAr_N$. $\delta\nu$-spectral shift and Γ linewidth (Ref. 15).
[f]Stokes shifts Eq. (15).

$$F_\nu(t)=\delta\nu_e(t)-\langle\delta\nu_e\rangle, \tag{22}$$

which was analyzed by Eqs. (3) and (4). In Table II we summarize the temporal and dynamic parameters $\{A_j\}$ $(j=0-3)$, $\tau_0=2^{1/2}\sigma$, $\{\tau_j\}$ $(j=1-3)$, $\{\omega_j\}$ and $\{\alpha_j\}$ $(j=2,3)$ emerging from the analysis of the time-dependent spectral shifts. A good fit of the $\delta\nu_e(t)$ data was obtained, as is evident from Figs. 5, 17, and 18.

The site-specific time-resolved emission spectroscopy of Xe^*Ar_{146} with the characteristic bubble formation for the interior (C), (1), and (2) Xe* sites and the spring formation for the surface (4)–(6) and (T) sites, exhibits the following features (Table II and Figures 5, 17, and 18):

(i) An initial Gaussian decay of $\delta\nu_e(t)$, with a characteristic time $\tau_0=2^{1/2}\sigma$ of 70 fs for the (C) site, ~120 fs for site (1), and ~130–140 fs for the surface sites (4) and (6). In spite of the substantial uncertainty in these τ_0 values two features of general trends emerge (Fig. 7 and Table II). Firstly, the values of τ_0 are somewhat lower for the spectral shift $\delta\nu_e(t)$ than for the configurational change $R^*_{NN}(t)$ (Sec. III). Secondly, the τ_0 values for the surface sites (4) and (6) seem to be somewhat longer than those for the interior site (C).

(ii) An exponential contribution $\tau_1\cong 1.5$ ps to the decay of $\delta\nu_e(t)$ for the (C) site, which is comparable to $\tau_1\cong 1.8$ ps for the time evolution of $R^*_{NN}(t)$ (Table II).

(iii) An oscillatory time dependence of $\delta\nu_e(t)$ at times $t>1$ ps for both interior and surface sites reflects vibrational coherence effects induced by the short range Xe*–Ar repulsions (see Sec. III). The frequencies for $R^*_{NN}(t)$ obtained from the FT of $F(t)$, Eq. (22), and the frequencies for $\delta\nu_e(t)$ obtained from the FT of $F_\nu(t)$, Eq. (3), are similar both for the interior (bubble) and for the surface (spring) sites (Fig. 19 and Table II).

(iv) The time-resolved spectral shifts for the surface sites (Figs. 17 and 18) [and in particular site (6)], which exhibit the spring effect, show an initial Gaussian decay (Secs. I, III, and IV) followed by a slow oscillatory decay to the asymptotic value with a damping lifetime of ~20 ps.

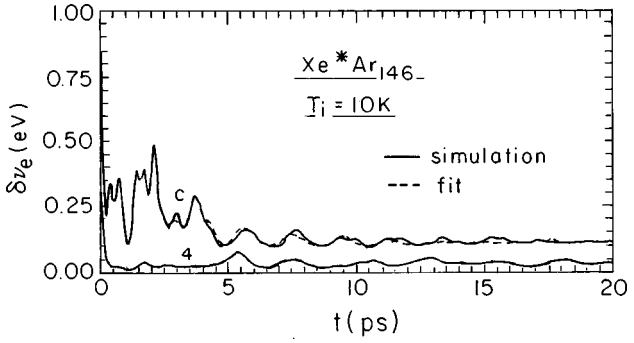

FIG. 17. Analysis of the time dependence of the spectral shift in emission using Eqs. (22) and (19) for the bubble central (C) Xe* site and for the spring Xe* surface site (6) (marked on the curves) in Xe^*Ar_{146} clusters at $T_i=10$ K. The parameters for the fits are given in Table II.

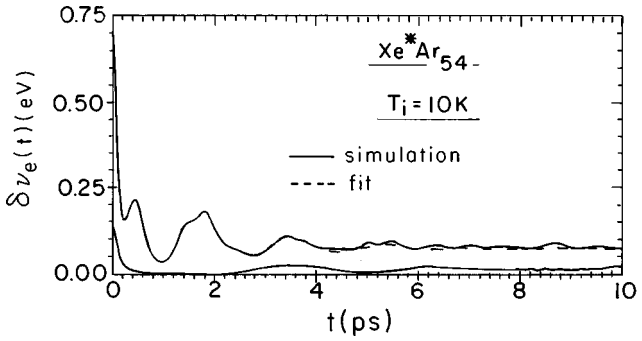

FIG. 18. Analysis of the time dependence of the spectral shifts in emission using Eqs. (22) and (19) for the bubble central Xe* site (C) and for the spring Xe* surface site (5) (marked on the curves) in Xe^*Ar_{54} clusters at $T_i=10$ K. The parameters for the fits are given in Table II.

In view of the similarity of the short-time structural relaxation dynamics in Xe^*Ar_{54} and Xe^*Ar_{146} clusters (Secs. III and IV), we expect similar results for short-time fluorescence ($t<10$ ps) for Xe^*Ar_{54} and Xe^*Ar_{146} clusters. $\delta\nu_e(t)$ data for Xe^*Ar_{54} are summarized in Figs. 5, 17, and 18 and in Table II for $T_i=10$ K. The initial Gaussian lifetimes τ_0 for the interior (C) and (I) sites and for the surface (O) and (V) sites of Xe^*Ar_{54} are close to the τ_0 values for the corresponding sites of Xe^*Ar_{146} (within the uncertainty of the fits), so that no marked cluster size effects on the ultrashort-time relaxation dynamics are exhibited. The characteristic frequencies for $\delta\nu_e(t)$ (Table II and Fig. 18) are again close to those for $R^*_{NN}(t)$. The damped oscillatory components of Xe^*Ar_{54} have lifetimes (2–3 ps) which are similar to those

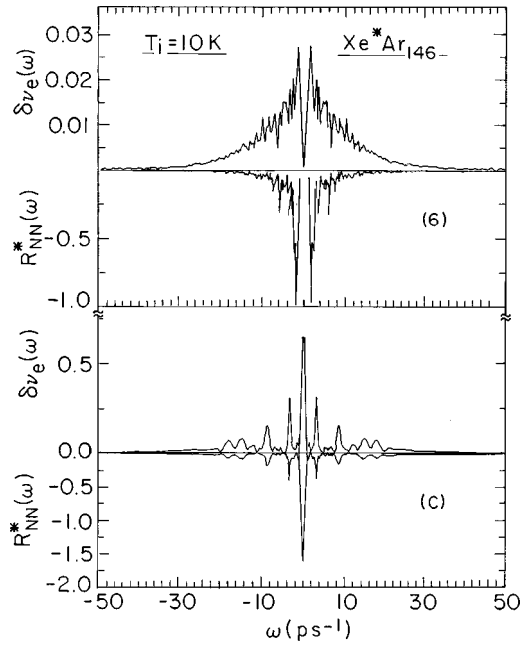

FIG. 19. The Fourier transforms $R^*_{NN}(\omega)=FT_\omega[R^*_{NN}(t)]$ and $\delta\nu_e(\omega)=FT_\omega[\delta\nu_e(t)]$ for the central (C) and surface (S) Xe* sites in Xe^*Ar_{146}. Note the near identity of the characteristic frequencies for the structural and spectroscopic temporal attributes.

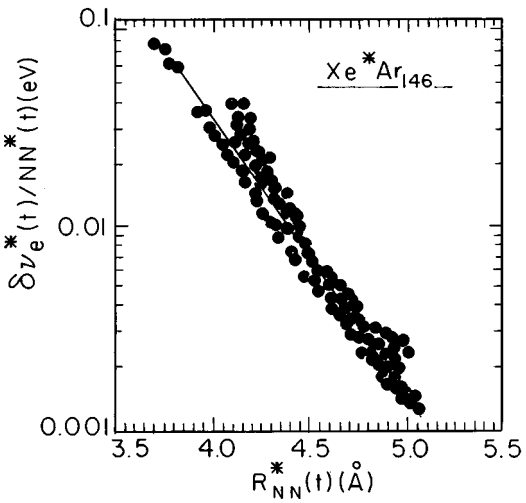

FIG. 20. A global analysis of the time dependent spectral shifts $\delta\nu_e(t)$ from the different Xe* sites (C), (1)–(6) in Xe^*Ar_{146} at the initial temperatures $T_i=10$ K, 30 K. The spectroscopic data over the broad range of parameters $\delta\nu_e(t)=0.92-0.01$ eV and over a wide range of the structural parameter $R^*_{NN}(t)=3.7-5.1$Å are well fit by the exponential spectrum structure relationship, Eq. (23), with the parameters $\gamma^*=3.06$Å^{-1} and $a^*=7.0\times10^3$ eV (solid line).

for Xe^*Ar_{146}. Long-time fluorescence ($t\sim100-10^3$ ps) from nonrigid Xe^*Ar_{54} clusters will be of considerable interest and will be discussed at the end of this section.

A spectrum-structure relation for the time-resolved emission spectral shifts can be provided. As the temporal spectral shift in emission is still dominated by the short-range repulsive interactions, it is expected to be extremely sensitive to the local microstructure. The short-range repulsive interactions are expected to depend roughly exponentially on the $Xe^*(^3P_1)$–Ar separation. Accordingly, we utilized an exponential nearest-neighbor distance relationship for the spectral shift, i.e.,

$$\delta\nu_e(t)=a^*[NN^*(t)]\exp[-\gamma^*R^*_{NN}(t)]. \tag{23}$$

We analyzed the time-resolved emission spectral shifts for both interior and surface Xe* sites in Xe^*Ar_{146} at $T_i=10$ K and 30 K, according to Eq. (23), with the values of $\delta\nu_e(t)$ spanning the range 0.92–0.01 eV, while the values of $R^*_{NN}(t)$ span the range 3.7–5.1 Å. From the plot of $\ln[\delta\nu_e(t)/NN^*(t)]$ vs $R^*_{NN}(t)$, for different initial interior and surface sites and at different times (Fig. 20), we infer that the exponential emission spectrum-structure relation, Eq. (23), is well obeyed, with the parameters $a^*=7.01\times10^3$ eV and $\gamma^*=3.06$ Å^{-1}. The parameters a^* and γ^* are very close to the parameters $a=(6.2\pm0.6)\cdot10^3$ eV and $\gamma=3.05\pm0.05$ Å^{-1} for the exponential absorption spectrum-structure relation.[15] This agreement provides a unified description of the structure-spectra relationship over a remarkably broad range of structural parameters, i.e., $R_{NN}=3.7-4.1$ Å for $\delta\nu$[15] and $R^*_{NN}(t)=3.7-5.1$ Å for $\delta\nu_e(t)$ for both absorption and emission.

For rigid large Xe^*Ar_{146} clusters (excited at $T_i\leqslant30$ K) the structural and spectroscopic dynamics is over at $t\gtrsim20$ ps, when the $\delta\nu_e(t)$ vs t curves converge to their asymptotic values $\langle\delta\nu_e\rangle$. The long-time behavior of $\delta\nu_e(t)$ for the excited (C) site of the nonrigid Xe^*Ar_{54} is rather complex, with the diffusion of the Xe* atom from the interior of the nonrigid cluster to its surface (Sec. IV). The time evolution of $\delta\nu_e(t)$ on the long-time scale reflects this behavior (Fig. 12), with the decrease of $\delta\nu_e(t)$ from 0.075 eV at $t=10$ ps to $\delta\nu_e(t)=0.02$ eV (i.e., a decrease by a numerical factor of 3.8) at $t=150$ ps. This decrease of $\delta\nu_e(t)$ reflects the change of the coordination number in the expanded configuration around Xe* from the interior dilated bubble structure for $t=10$ ps with NN* (10 ps) = 16.5 to the surface spring structure at $t=150$ ps with NN* (150 ps) $\cong$ 4.7 (Fig. 12). According to Eq. (23) we expect that (for fixed R^*_{NN}) the spectral shift at $t=150-200$ ps will be reduced by a numerical factor of 3.5, in accord with the $\delta\nu_e(t)$ data of Fig. 12.

What is the feasibility of the spectroscopic interrogation of the energy-resolved fluorescence? For a large cluster, i.e., Xe^*Ar_{146}, the rigid cluster undergoes nondissociative intracluster configurational relaxation. For the (C) bubble expansion the relevant time scales for the occurrence of marked changes in $\delta\nu_e(t)$ are (Fig. 17 and Table II) the ultrashort time $\tau_0\cong70$ fs and $\tau_1\cong1.5$ ps, followed by the decay of the oscillatory components of τ_2, $\tau_3\cong2-4$ ps. The radiative lifetime of the $Xe^*(^3P_1)$ state is 3–5 ns.[19] Accordingly, the fluorescence quantum yields during the evolution of the time-resolved fluorescence are $\sim2\times10^{-5}$ for τ_0, $\sim4\times10^{-4}$ for τ_1 and $\sim10^{-3}$ for τ_2,τ_3. Similar fluorescence quantum yields will be exhibited for τ_0 and τ_2, τ_3 from other interior and surface states of Xe^*Ar_{146}. Such low-yield time-resolved fluorescence can be interrogated by fs laser-

induced fluorescence upconversion studies, which constitute a difficult experiment in the vacuum ultraviolet spectral domain. An alternative experimental approach will involve the time-resolved absorption of the $Xe^*(^3P_1)$ state in clusters, i.e., interrogating the Xe $6s[3/2]_1 \rightarrow np,s,d[3/2,5/2]_{0,2}$ transitions of the Xe guest atom by fs laser-pump-probe experiments. Note that this atomic description of the electronic excitation of Xe in a cluster is probably justified for $n=6,7$, according to the experimental correlation diagrams of Messing *et al.*[18]

The situation is different for medium-sized Xe^*Ar_{54} clusters, with Xe* at the (C) site, which loses its rigidity but maintains its integrity. The short time-resolved fluorescence on the time scale of ~ 10 ps (Fig. 18) is similar to that of the larger Xe^*Ar_{146} cluster (Fig. 17) although its damped oscillatory components have a shorter lifetime. However, the time-resolved emission of the nonrigid Xe^*Ar_{54} cluster on a long-time scale of ~ 200 ps will allow for the monitoring of the global structural cluster change with the interior Xe* bubble site being transferred to the surface Xe* spring on a time scale of $t \sim 150$ ps (Fig. 12). The interrogation of the time-resolved spectral shift (or Stokes shift) in the fluorescence of Xe^*Ar_{54} on the time scale of ~ 500 ps, according to the prediction of Fig. 12, will constitute a relatively easy experiment, which will provide useful information on mass transport of the Xe* bubble.

The exploration of excited-state fs and ps configuration changes in Xe^*Ar_N ($N=54$, 146) clusters by the interrogation of time-resolved fluorescence and transient absorption constitutes a real experimental challenge. Useful, though considerably less complete, information of these configuration changes emerges from energy-resolved total fluorescence spectra.

VII. ENERGY-RESOLVED FLUORESCENCE SPECTRA OF Xe^*Ar_{146}

We have calculated the long-time fluorescence spectra $L_e(E)$, Eq. (11), of Xe^*Ar_{146} clusters using the spectral density method (Sec. II D). The configurational relaxation in these rigid clusters occurs on the time scale of $t \leqslant 20$ ps, whereupon the fluorescence quantum yield during the configurational relaxation process is negligible. The simulated emission line shapes (Fig. 21) at $T_i=10$ K and $T_i=30$ K correspond to the average temperatures $\langle T^* \rangle$ tabulated in Table III. The power spectra for the emission bands are analyzed in the Appendix. The line shapes are Gaussian, corresponding to the Kubo slow modulation limit.[51] In Table III we summarize the asymptotic spectral shifts $\langle \delta \nu_e \rangle$, and the linewidths Γ_e (see Sec. II D) of the fluorescence bands. The strong modulation limit is reflected in the temperature dependence of the linewidth $\Gamma_e \propto \langle T^* \rangle^{1/2}$. The simulated Γ_e data obtained from the line shapes of Fig. 21 confirm this relation with the $\langle T^* \rangle$ data given in Table III. The spectral features for the emission bands for Xe^*Ar_{146} are compared in Table III with the corresponding spectral features, i.e., the spectral shift $\delta \nu$ and the linewidth (FWHM) Γ at the temperature for absorption $T_i=30$ K. The following predictions emerge:

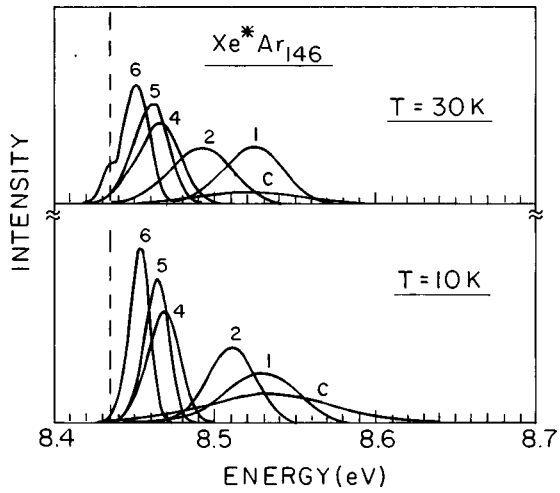

FIG. 21. Simulated site-specific emission line shapes for Xe^*Ar_{146} clusters. The sites are marked on the curves. The initial cluster temperatures are $T_i=10$ K and $T_i=30$ K (as marked on the panels) while the cluster temperatures $\langle T^* \rangle$ are given from Table I. All line shapes are normalized to unity.

(1) The $Xe^*(^3P_1)$ atom is bound for all sites on the ns time scale.
(2) The long-time emission spectra are characterized by small blue spectral shifts ($\langle \delta \nu_e \rangle = 0.01-0.1$ eV).
(3) The emission spectral shifts $\langle \delta \nu_e \rangle$ exhibit a site specificity, with the hierarchy $\langle \delta \nu_e \rangle(C) > \langle \delta \nu_e \rangle(1) \gtrsim \langle \delta \nu_e \rangle(2) \gtrsim \langle \delta \nu_e \rangle(3) > \langle \delta \nu_e \rangle(4) > \langle \delta \nu_e \rangle(5) > \langle \delta \nu_e \rangle(6) \gtrsim \langle \delta \nu_e \rangle(T)$. This hierarchy reflects the decrease of local cluster perturbations for the equilibrated excited electronic state in decreasing order from the (C) bubble to the internal bubble and to the surface spring. This hierarchy of the emission energetics is qualitatively similar to that in absorption,[15] where the perturbations of the Xe microenvironment are considerably stronger (Table III). The (blue) spectral shifts $\langle \delta \nu_e \rangle$ in emission are considerably smaller than the corresponding spectral shifts $\delta \nu$ in absorption.
(4) Large Stokes shifts between the peaks of the absorption and emission spectra are predicted (Table III). The large Stokes shifts reflect the marked reductions of the microenvironment perturbation of Xe* in the configurationally relaxed excited state. These Stokes shifts are site specific, exhibiting in the hierarchy SS(central) >SS(internal)>SS(surface)$\gtrsim$SS(top).
(5) The linewidths Γ_e follow the site-specific order of the shifts. The values of Γ_e reflect again the hierarchy of central bubble, internal bubble, and surface spring. The emission linewidths are considerably lower than the corresponding site specific linewidths in absorption (Table III).
(6) The hierarchy of large Stokes shifts and of the reduced line broadening in emission relative to absorption provides the long-time manifestation of the formation of the bubble for the (C), (1), and (2) sites and the spring for the surface (4)–(6) and (T) sites.
(7) Universality. Size invariant characteristics of $\langle \delta \nu_e \rangle$ and Γ_e were obtained for large $N=146$ and $N=199$ clusters,

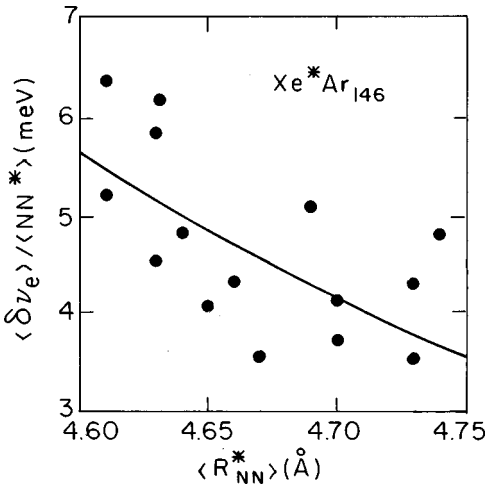

FIG. 22. The long-time asymptotic spectral shifts $\langle \delta\nu_e \rangle$ of the emission bands from different Xe* sites in Xe^*Ar_{146} clusters excited at $T_i = 10$ K and 30 K, can be reasonably well accounted for in terms of the spectral-structure relationship, Eq. (23), with $\gamma^* = 3.0 \text{Å}^{-1}$ and $a^* = 6.0 \times 10^3$ eV (solid line).

pointing towards site-specific cluster size independent spectral features in emission.

These simulated data will be confronted in Sec. VIII with the available spectroscopic results.[11–14]

The calculated site-specific ('long-time') asymptotic emission (blue) spectral shifts $\langle \delta\nu_e \rangle$ of large Xe^*Ar_{146} clusters (Table III) are characterized by relatively low values of $\langle \delta\nu_e \rangle = 0.01 - 0.1$ eV. These small values of $\langle \delta\nu_e \rangle$ correspond to the spectral shift of the Xe* atom in a fully dilated bubble for (C), (1), (2) or for a fully stretched spring for (4)–(6) and (T) initial Xe* sites. While the $\langle \delta\nu_e \rangle$ values for different sites of Xe^*Ar_{146} vary by about one order of magnitude, the reduced parameter $\langle \delta\nu_e \rangle$/NN* reveals a considerably weaker variation (50%). The exponential structure-emission spectral relationship, Eq. (23), for the asymptotic spectral shifts in the relaxed structure does hold (though with a considerable scatter of the data) for the asymptotic spectral shifts. In Fig. 22 we plot $\ln[\langle \delta\nu_e \rangle / \langle \text{NN}^* \rangle]$ vs $\langle R^*_{\text{NN}} \rangle$, according to Eq. (23), demonstrating that the relation $\langle \delta\nu_e \rangle = a^* \exp(-\gamma^* \langle R^*_{\text{NN}} \rangle)$, with the exponential parameter $\gamma^* \cong 3 \text{ Å}^{-1}$, and $a^* = 6 \times 10^3$ eV is reasonably well obeyed. Both the time-dependent $\delta\nu_e(t)$ data and the asymptotic $\langle \delta\nu_e \rangle$ values, are accounted for in terms of a single structure-spectral relationship, Eq. (23), with the same parameters.

VIII. CONFRONTATION WITH EXPERIMENTAL FLUORESCENCE SPECTRA

Möller and his colleagues[11] provided the first experimental study of the spectrally resolved fluorescence of Xe^*Ar_{1400} clusters following photoselective excitation of site-selective central (C), interior (I), and surface (S) absorption bands. The temperature of these $XeAr_{1400}$ clusters, as inferred from our analysis of the absorption spectra,[15] was $T_i \cong 30$ K. The following results were reported:[11]

(1) Excitation of the Xe atom of the central (C) site ($E = 9.22$ eV, $\delta\nu = 0.78$ eV) leads to a prominent emission band at $E = 8.43$ eV $[\langle \delta\nu_e \rangle(\text{expt}) = 0.01 \pm 0.004$ eV] with two additional weak emission bands at $E = 8.62$ eV and at $E = 8.85$ eV.
(2) Excitation of an interior (I) Xe site(s) ($E = 9.05$ eV, $\delta\nu = 0.62$ eV) results in a prominent emission band peaking at $E = 8.43$ eV $[\langle \delta\nu_e \rangle(\text{expt}) = -0.001 \pm 0.004$ eV], with a weaker emission band at $E \cong 8.62$ eV.
(3) Excitation of the surface (S) Xe sites ($E = 8.65$ eV, $\delta\nu = 0.21$ eV) results in a prominent emission band at 8.45 eV ($\langle \delta\nu_e \rangle = 0 \pm 0.004$ eV).

We shall focus on the prominent emission bands. The most dramatic general feature of the experimental site-specific spectroscopy of $XeAr_N$ clusters pertains to the small spectral shifts $\langle \delta\nu_e \rangle$ in emission, in contrast to the large spectral blue shifts $\delta\nu$ in absorption, which result in large Stokes shifts (Table IV). According to our simulations, these spectroscopic effects manifest the substantial configurational relaxation around the impurity extravalence electronic relaxation. The small experimental $|\langle \delta\nu_e \rangle|$ and large $\langle \text{SS} \rangle$ values for the (C) and (I) sites (Table IV) are in semiquantitative agreement with our predictions regarding the bubble formation, while the experimental zero spectral shift in emission of the (S) site (Table IV) is consistent with our prediction for the spring formation. In Fig. 23 and Table IV we compare Möller's experimental results for the prominent emission bands[11] in Xe^*Ar_{1400} with theoretical data for Xe^*Ar_{146}. The rather bold extrapolation of the spectroscopic information from $N = 146$ to $N = 1400$ rests on the weak size dependence of the $XeAr_N$ ($N = 120 - 200$) absorption spectra[15] and on the comparison between the simulated data for emission spectra of $N = 146$ and $N = 199$ clusters, which indicate that the spectroscopic features of the (C), (I), and (S) sites in large clusters are almost cluster size invariant.

TABLE IV. Experimental (Ref. 11) and theoretical asymptotic long-time spectroscopic observables for the emission spectra of large Xe^*Ar_N clusters (all data in eV).

Site	$\langle \delta\nu_e \rangle$ Expt.[a]	$\langle \delta\nu_e \rangle$ Calc.[b,c]	$\langle \text{SS} \rangle$ Expt.[a]	$\langle \text{SS} \rangle$ Calc.[b,c]	Γ_e Expt.[a,d]	Γ_e Calc.[b,c]
(C)	-0.010 ± 0.004	0.09	0.9	0.7	0.1	0.09
(I)	-0.010 ± 0.004	0.02–0.06	0.7	0.4–0.5	0.06	0.045
(S)	0 ± 0.004	0.02–0.03	0.3	0.1–0.2	0.03	0.02

[a] $N = 1400$ (Ref. 11).
[b] $N = 146$ (present work).
[c] $T_i = 30$ K.
[d] Experimental linewidth is not corrected for the spectral resolution.

The overall agreement between our theoretical results and the experimental[11] features of the energetics $\langle \delta\nu_e \rangle$ and the line broadening Γ_e of the site-specific emission spectra is satisfactory (Fig. 23 and Table IV). The calculated and experimental spectral shifts $\langle \delta\nu_e \rangle$, with the hierarchy $\langle \delta\nu_e \rangle(\mathrm{C}) > \langle \delta\nu_e \rangle(\mathrm{I}) > \langle \delta\nu_e \rangle(\mathrm{S})$, provide support for our picture of excited-state configurational relaxation, i.e., the bubble formation for the interior (C) and (I) sites and the spring stretching for the surface (S) sites. The calculated linewidths Γ_e reveal a hierarchy $\Gamma_e(\mathrm{C}) > \Gamma_e(\mathrm{I}) > \Gamma_e(\mathrm{S})$, in accord with the experimental data (Table IV). The agreement between the calculated and the experimental Γ_e values for the (C), (I), and (S) (excited at $T_i = 30$ K) sites is quite good, being within 10%–30% (Table IV). The experimental results for Γ_e, which are somewhat larger than the calculated data, also reflect ''trivial'' spectral resolution effects in conjunction with possible inhomogeneous line broadening effects for the experimental emission spectra.[11] In particular, the (S) and (I) sites will reflect a hierarchy of linewidths. In relation to the (S) site, the narrow bandwidth and the experimental negligible emission spectral shift[11] are not attributed to dissociation of Xe*, but rather to small local perturbations in the spring surface site.

The results of our calculations for the spectral shifts and linewidths in emission provide a reasonable, but only a semiquantitative, description of the spectroscopic manifestations of the large cluster configurational dilation around the Xe* Rydberg excitations. The agreement between the calculated and the experimental linewidths is reasonable, although one should worry about the asymmetric experimental linewidths for the (I) and (S) sites (Fig. 23), in contrast to the theoretical prediction of a symmetric Gaussian line shape in the strong modulation limit. Regarding energetics, as is evident from Table IV, the large Stokes shifts are well accounted for. A more pedantic scrutiny reveals that the calculated $\langle \delta\nu_e \rangle$ values for the (C) and (I) sites are of the opposite sign relative to the corresponding experimental $\langle \delta\nu_e \rangle$ values (Table IV and Fig. 23), although both experimental and calculated $\langle \delta\nu_e \rangle$ values are very small. This discrepancy between theory and experiment may presumably reflect the limitations in our description of the long-range excited state potential at large separations, or rather of the asymptotic form of the potential difference $\Delta V(r) = V_e(r) - V_g(r)$ between pair potentials in the electronically excited state and in the ground state.

Some open questions regarding excited state dynamics of Xe^*Ar_N clusters still remain. We are unable to explain the long lifetime (~ 100 ns) reported by Möller *et al.*[12] for the emission from the (C) site, although this long-lived emission may originate from the 8.62 eV and 8.85 eV bands, which may have parentage in metastable $Xe^*(^3P_2)$ or excimer Xe_2^* excitations. We are also unable to explain the auxiliary emission bands, i.e., the 8.62 eV emission band from the (S) site and the 8.62 eV and 8.85 eV emission bands from the (C) sites[11] (Fig. 23). These auxiliary emission bands may be due to metastable Xe* excitations, to Xe_2^*, or to interstitial Xe trapping sites in very large clusters. What is important is that our overall picture regarding the spectroscopic implications

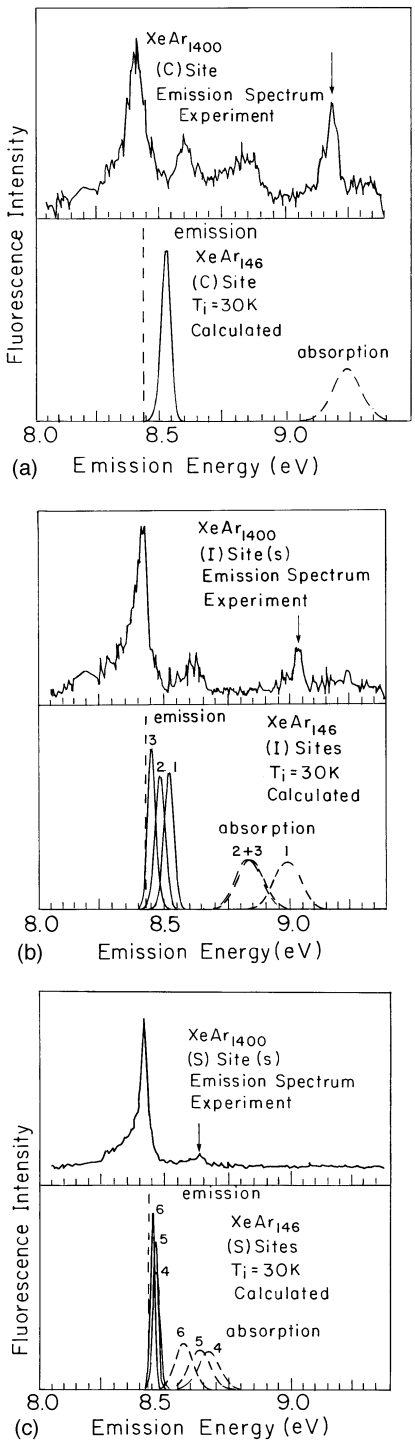

FIG. 23. A comparison between the simulated site-specific line shapes in the emission spectra (—) of Xe^*Ar_{146} at $T_i = 30$ K (lower panel) and the experimental emission spectra of Xe^*Ar_{1400} (upper panel) reported by Möller *et al.* (Ref. 11). In each of the experimental energy-resolved spectra (Ref. 11) the excitation energy is marked by an arrow. In the lower panel the simulated absorption spectra (---) are also given and they are close in energy to the strong-light band in the emission spectra reproduced in the upper panel. Each of the calculated emission bands and absorption bands of Xe^*Ar_{146} are marked by the specific Xe* site. (a) Xe* atom in central (C) site. (b) Xe* atom in interior (I) sites (1)–(3). (c) Xe* atom in surface (S) sites (4)–(6).

TABLE V. Relaxation dynamics of interior and surface Xe* sites in Xe^*Ar_{146} ($T_i = 10$ K).

	Bubble	Spring	
	Site (C)	Site (4)	Site (6)
τ_{ET} (fs)[a,b]	60	80	80
τ_0 (fs)[c,b]	170	280	210
τ_1 (ps)[d]	2	-	-
τ_D (ps)[e]	4	1.5	1.5
$\langle R^*_{NN}\rangle - R^*_{NN}(0)$ (Å)[f]	0.82	0.60	0.60
$\langle NN^*\rangle - NN^*(0)$[f]	5.5	−1.0	0
$\langle R^*_{CM}\rangle - R^*_{CM}(0)$ (Å)[f]	3.9	1.4	0.84
Frequencies ω_2, ω_3 (cm^{-1})[g]	17, 40	17, 37	10
Damping times τ_2, τ_3 (ps)[g]	2.0, 6.0	2.5, 4.0	(20)[h]

[a]Energy flow into cluster.
[b]Gaussian time dependence.
[c]Initial configurational relaxation.
[d]Exponential time dependence.
[e]Dislocation time of Xe* to 90% initial rise of $R^*_{CM}(t)$.
[f]Asymptotic long-time structural data.
[g]Impact vibrational coherence of $R^*_{NN}(t)$.
[h]Entry in parentheses represents larger uncertainty (50%).

of the large excited-state configurational relaxations are borne out by experiment.

IX. CONCLUDING REMARKS

We were concerned with structural, spectroscopic, and dynamic manifestations of large local configurational changes induced by extravalence Rydberg excitation of a probe atom (e.g., the $^1S_0 \rightarrow {}^3P_1$ excitation of Xe) in a rare-gas cluster. Site-specific cluster dynamics with a fixed size Xe^*Ar_N cluster and size-specific cluster dynamics for small ($N=12$), medium size ($N=54$), and large ($N=146,199$) clusters were explored. Regarding site-specific cluster dynamics, our MD simulations provide evidence for large configurational dilation, resulting in a bubble formation for interior sites and a spring formation for surface sites. In the analysis of the bubble and of the spring dynamics it will be instructive to compare the time scales to the lower limit for the characteristic time $\tau_{VIB} = 1/c\omega_{VIB}$ of the cluster vibrational motion, where $\omega_{VIB} \cong 50\ cm^{-1}$ is the upper limit of the cluster frequency spectrum, i.e., $\tau_{VIB} \cong 700$ fs. For the interior sites [e.g., sites (C), (1), and (2) in Xe^*Ar_{146}], the life story of the bubble (summarized in Table V) is as follows. Ultrashort energy transfer to the cluster occurs on the time scale of $\tau_{ET} \cong 60$ fs. As $\tau_{ET} \ll \tau_{VIB}$ the vibrational nuclear motion of the cluster is frozen on the time scale of the initial impact induced energy transfer to the cluster. The subsequent time evolution of the bubble configurational relaxation is multimodal, being characterized by an initial ultrafast configurational dilation with a characteristic (Gaussian) time $\tau_0 \cong 170$ fs, followed by a longer (exponential) lifetime $\tau_1 \cong 2$ ps. The initial bubble expansion is characterized by $\tau_0 < \tau_{VIB}$, whereupon the inertial radial expansion with Gaussian time-dependence occurs on a time scale faster than cluster vibrational motion. The longer exponential expansion time, $\tau_1 < \tau_{VIB}$, manifests bubble expansion on the time scale of cluster vibrational motion. At the time scale the relative increase of the bubble radius, Eq. (17), is $f(\tau_1) \cong 0.9-1.1$. The subsequent bubble expansion is also accompanied by the dislocation of the Xe* bubble on a time scale of $\tau_D \cong 4$ ps. The short-range repulsive Rydberg-host atom interactions which drive the bubble formation induce vibrational coherence effects with characteristic frequencies of $\omega_2 \sim 40\ cm^{-1}$ and $\omega_3 \sim 20\ cm^{-1}$ with the damping (dephasing) times of $\tau_2 \sim 2$ ps and $\tau_3 \sim 6$ ps, respectively. The vibrational modes ω_2 and ω_3 fall in the range of cluster vibrational frequencies. The characteristic times for these vibrational modes $1/c\omega_2 = 800$ fs and $1/c\omega_3 = 1.6$ ps are shorter than or comparable to the damping times τ_2 and τ_3. After ~ 10 ps the bubble reaches its new equilibrium configuration ($\Delta R^*_b = 0.7-0.8$ Å) on the excited state potential surface. The spring formation [e.g., site (6) of Xe* in Xe^*Ar_{146}] is induced by ultrafast energy transfer $\tau_{ET} \cong 80$ fs (with $\tau_{ET} \ll \tau_{VIB}$) and is also characterized by a multimodal time evolution (see Table V). The initial Gaussian spring stretching time is $\tau_0 \cong 210$ fs. Also for the initial radial motion of the spring $\tau_0 < \tau_{VIB}$, manifesting inertial motion. This is followed by spring configurational relaxation, which exhibits substantial stretching with $R^*_{NN}(t)$ reaching a maximum value at $t = \tau_M \cong 1.3-2.0$ ps, with a substantial relative increase of the spring size, Eq. (17), being $f(\tau_M) \cong 2.0$. Subsequently the spring contracts, with the relaxation process taking place on a long-time scale of ~ 20 ps, with vibrational coherence with a characteristic frequency of $\omega_2 \sim 10\ cm^{-1}$, being induced. The overall spring stretching is characterized by $\Delta R^*_s = \langle R^*_{NN}\rangle - R^*_{NN} = 0.6$ Å.

Several new dynamic aspects of the configurational relaxation induced by the short-range Rydberg-host atoms repulsive interactions emerge:

(1) The initial ultrafast impact-induced energy transfer to the cluster occurs on the time scale $\tau_{ET} \ll \tau_{VIB}$, with the vibrational nuclear motion of the cluster being frozen. This ultrafast (Gaussian) time evolution for initial energy flow prevails for all interior and surface sites.
(2) The configurational relaxation is indeed driven by the initial impact energy flow, as $\tau_0 < \tau_{ET}$.
(3) The Gaussian time evolution for initial configurational relaxation on the time scale $\tau_0 < \tau_{VIB}$ manifests radial inertial short-time bubble expansion or spring stretching. Such radial, Gaussian time evolution for configurational relaxation bears analogy to the features of inertial, short-time solvation dynamics in polar solvents.[53–56] The Gaussian temporal form of the ultrashort time evolution is general, being manifested for all interior and surface sites.
(4) The longer exponential configurational relaxation times $\tau_1 > \tau_{VIB}$ of the bubble and of the spring occur on the time scale slower than or comparable to the cluster vibrational motion.
(5) Impact induced vibrational coherent excitation is manifested both for the bubble expansion and for the spring dynamics. This vibrational coherence, induced by the short-range repulsive interactions on the ultrashort time scale $\tau_{ET} \ll \tau_{VIB}$, manifests the excitation of a vibrational

wave packet. The energy range for the impact excitation $\hbar/\tau_{ET} \cong 100\ cm^{-1}$ is sufficiently large to excite a wave packet of the cluster vibrations. The wave packet is characterized by frequencies ω_2, ω_3, which fall in the range of the cluster vibrational frequencies, i.e., ω_2, $\omega_3 \leqslant \omega_{VIB}$. The ps lifetimes τ_2, τ_3 for damping of the wave packet are comparable to or longer than the characteristic life times for the cluster vibrational motion.

(6) The interior site bubble dynamics and the surface site spring dynamics qualitatively differ in their overall time evolution of $R^*_{NN}(t)$ and in the damping of the vibrational coherence.

Regarding dynamic size effects we have established that large Xe^*Ar_{146} clusters maintain their integrity on the relevant (ns) time scale and maintain rigidity under reasonable experimental conditions, i.e., $T_i \leqslant 30$ K. Medium-sized Xe^*Ar_{54} clusters maintain their integrity on the relevant (ns) time scale, but the (C) site excitation induces the loss of cluster rigidity, with the Xe* bubble being utilized as a spectroscopic probe for long-time (100–200 ps) mass transport from the interior bubble to the surface spring. Finally, small Xe^*Ar_{12} clusters exhibit reactive dissociative dynamics. It was previously established that high-energy vibrational excitation of a probe molecule[21,22,60] in a cluster exhibits a transition from molecular-type dissociative dynamics in small clusters to condensed phase nonreactive vibrational relaxation in large clusters and manifests the bridging between molecular and condensed phase nuclear dynamics.[4] The relaxation of Xe^*Ar_N clusters explored herein provides a generalization of dynamic cluster size effects for configurational relaxation induced by short-range atom–atom repulsion due to extravalence electronic excitation. This configurational change involves site-specific and size-specific dissociative or nonreactive dynamics. The transition from molecular to condensed phase dynamics involves dissociative dynamics in small clusters, nonreactive configurational and mass-transport dynamics in nonrigid medium-sized clusters and nonreactive configurational dynamics in rigid large clusters. It is significant that our analysis provides ways for the interrogation of these dynamic size effects by time-resolved fs and ps cluster spectroscopy.

Our analysis of the time-resolved and long-time optical emission spectroscopy of Xe^*Ar_N clusters constitutes a bridge between cluster spectroscopy and dynamics. Energy-resolved emission line shapes provide coarse grained information on the relaxation dynamics. These involve site-specific small spectral shifts $\langle \delta\nu_e \rangle$, large Stokes shifts and rather small emission linewidths. The general picture emerging from these spectroscopic data is in accord with our predictions for the manifestations of large configurational changes. Much more instructive will be the time-resolved fs and ps ultrafast fluorescence spectroscopy. Of course, time-resolved fluorescence constitutes just one method in the experimental arsenal of femtosecond pump-probe time-resolved spectroscopy,[61,62] which can be used to interrogate structural relaxation induced by extravalence electronic excitations in heteroclusters.

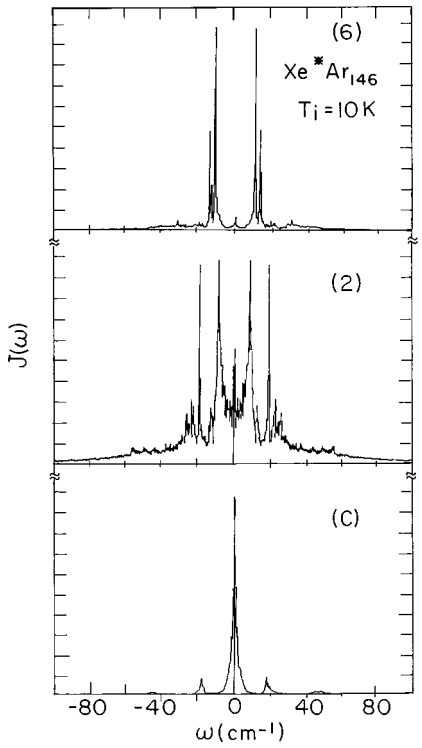

FIG. 24. The power spectra $J(\omega) = FT_\omega[J_e(t)]$, where J_e is given by Eq. (10), for the emission spectra of Xe^*Ar_{146} in the central (C), interior (2), and surface (6) Xe* sites (marked on the panel). Initial cluster temperature $T_i = 10$ K.

The structural relaxation induced by an extravalence Rydberg excitation of a probe atom or molecule in a rare-gas cluster manifests the implications of the short-range Pauli repulsion between the spatially extended Rydberg wave function of the probe and the host atoms. Our results for cluster dynamics are of considerable significance for the spectroscopy and structural relaxation of Rydberg states of atoms and molecules in the condensed phase.[19,63,64] Some implications of the prevalence of short-range repulsive interactions between extravalence excitations of a probe atom [e.g., Xe (Ref. 19)] or molecule [e.g., NO (Refs. 63 and 64)] and the host atoms in a rare-gas solid, liquid, or fluid can be inferred from energy-resolved spectroscopy.[19,63] (i) Absorption spectroscopy. Large blue spectral shifts of up to ~1 eV in absorption (relative to the isolated atom) manifest short-range repulsive interactions in the nuclear configuration of the ground electronic state. (ii) Fluorescence spectroscopy. Large Stokes shifts, up to ~1 eV, of the fluorescence spectra reflect large configurational dilation in the excited state on a time scale which is considerably shorter than the (ns) excited state life time. Our simulations for the dynamics of the probe Xe atom in the central (C) and interior sites of Ar clusters are pertinent for the elucidation of the ultrafast dynamics of atomic and molecular Rydberg excitations in the condensed phase.[19,63,64] The general features of the multimodal time evolution of the bubble formation with the time scales $\tau_0 \cong 200$ fs, $\tau_1 \cong 2$ ps, and τ_2, $\tau_3 = 2-6$ ps, in conjunction with the predictions of vibrational coherence obtained herein for the (C) site of the large Xe^*Ar_{146} cluster, provide guidelines

TABLE VI. Parametrization of the power spectra $J(\omega)$ of Xe^*Ar_N clusters.

N	Site	T_i (K)	j	ω_j (cm^{-1})[a]	γ_j (cm^{-1})[a]	Δ_j^2 (10^6 cm^{-2})[a]	Δ (cm^{-1})[b]	Δ/γ_1 Δ/ω_j $(j\neq 1)$
146	(C)	10	1	0	1.4	241.1		134
			2	16.3	1.6	37.2	188	118
			3	44.0	4.2	19.3		45
146	(C)	30	1	0	1.0	635.8		290
			2	17.9	1.2	68.2		16
			3	45.6	1.8	25.4	291	6
			4	78.2	1.2	7.0		4
			5	96.1	0.6	3.6		3
146	Interior (2)	10	1	0	0.7	8.7		158
			2	6.5	1.4	22.6		17
			3	11.4	0.5	3.7		10
			4	17.9	0.5	6.6	111	6
			5	21.2	0.4	2.8		5
			6	26.1	0.4	2.6		4
			7	29.3	0.8	2.6		4
			8	32.6	0.8	1.7		3
			9	37.5	1.1	2.2		3
			10	44.0	1.0	1.7		3
			11	48.9	1.2	2.2		2
			12	53.7	0.9	1.8		2
			13	71.7	9.8	6.5		2
146	Surface (5)	10	1	0	1.4	0.7		44
			2	6.5	0.2	4.5		9
			3	8.1	0.2	2.2		8
			4	13.0	0.3	2.1		5
			5	17.9	0.7	1.7	61	3
			6	22.8	1.1	2.1		3
			7	27.7	0.8	2.0		2
			8	42.3	7.5	3.8		1
146	Surface (6)	30	1	0	0.9	2.6		71
			2	8.1	0.6	6.0		8
			3	11.4	0.6	4.3		6
			4	14.7	0.8	1.2	64	4
			5	19.5	1.3	1.7		3
			6	26.1	1.8	2.1		2
			7	30.9	2.5	1.9		2
			8	52.1	6.9	2.1		1

[a]Parameters from power spectra.
[b]$\Delta=[\Sigma_{j=1}^{L}\Delta_j^2]^{1/2}$.

for the structural relaxation dynamics of atomic and molecular Rydbergs in solid rare gases. In a recent experimental study of the ultrafast dynamics of bubble formation around the $A\ ^2\Sigma^+ 3s\sigma\ (v=0)$ Rydberg excitation of NO in solid Ar at 5 K, Chergui *et al.*[64] provided evidence for the formation of the bubble on the time scale of 4–5 ps. This result is in accord with our predictions for the longer relaxation times for the bubble formation in the central site in Xe^*Ar_{146}, which give $\tau_1\cong 2$ ps, $\tau_2\cong 2$ ps, and $\tau_3\cong 6$ ps, with the time scale for the completion of the bubble relaxation being ~ 10 ps. No experimental evidence for the ultrashort $\tau_0=200$ fs relaxation time and for the vibrational coherence effects is currently available. On the theoretical front the simulations described herein for finite systems have to be extended for the relaxation dynamics in condensed macroscopic rare gases (solids and fluids), providing another avenue for the merging between molecular and condensed phase dynamics. Our theoretical studies and their extensions for solid and liquid rare gases are expected to provide guidance, predictions, and insight for important time-resolved experiments[64] on the fate of Rydberg states in clusters and in the condensed phase.

ACKNOWLEDGMENTS

We are grateful to Professor Majed Chergui and Dr. Thomas Möller for stimulating discussions and correspondence and for prepublication information. This research was supported by the German–Israel Binational James Franck Program on Laser-Matter Interaction.

APPENDIX: POWER SPECTRA OF THE EMISSION BANDS

To understand different sources of the line shape broadening, the power spectra for the emission bands were ana-

lyzed. Characteristic power spectra for different Xe* atom sites in the Xe^*Ar_{146} cluster are shown in Fig. 24. These power spectra are represented in terms of the superposition of Lorentzians,[15,20] whereupon the energy gap autocorrelation function is represented in terms of the superposition of dumped oscillators with frequencies $\{\omega_j\}$, dampings $\{\gamma_j\}$, and dispersions $\{\Delta_j\}$ as described in our previous article[15] [see Eqs. (12.1)–(12.6) of Ref. 15]. Information on the power spectra pertains to the nuclear dynamics, which is manifested in the spectral line broadening. We consider the classical power spectrum which is symmetric, i.e., $J_e(\omega) = J_e(-\omega)$. In Fig. 24 typical power spectra (for excitation at $T_i = 10$ K) are presented. The simulated power spectra $J(\omega)$ were fit by using Mukamel's approach,[24–31] Eq. (12.4) of Ref. 15. A sample of the parameters is given in Table VI. At a constant initial temperature the number L of the modes (with the frequency peaks in the power spectrum being numbered as 1,...,L) increases with the Xe* atom being moved away from the center of mass of the cluster. Concurrently, the dispersion (relative intensity) Δ_1^2 of the soft mode (i.e., the zero frequency line $\omega_1 = 0$ in Table VI) assumes the highest value for the (C) sites and obeys the hierarchy $\Delta_1^2(C) > \Delta_1^2(1) > \Delta_1^2(2) > \Delta_1^2(3) > \Delta_1^2(4) > \Delta_1^2(5) > \Delta_1^2(6)$, gradually decreasing for the interior sites (1)–(3) and becoming small for the surface sites (4)–(6) (Table VI). The total dispersions Δ^2 at fixed T_i also decrease gradually from the (C) site towards the interior sites (1)–(3) and towards the surface sites (4)–(6) (Table VI) with the decrease of the emission spectral linewidths, according to the hierarchy of Γ_e, observed in Sec. VII. The finite frequency peaks $\{\omega_j\}$ ($j = 2,...,L$), with characteristic vibrations $\omega_j = 3-80\ \mathrm{cm}^{-1}$, represent intracluster vibrations with characteristic dephasing times of $\tau_j = 5-0.5$ ps ($\gamma_j = \hbar\tau_j^{-1} = 1-10\ \mathrm{cm}^{-1}$). In terms of Kubo's[51] and Mukamel's[24–31] line broadening formalism these emission line shapes correspond to the slow modulation limit. For the soft mode the slow modulation (short-time) limit is realized[15] when the total dispersion $\Delta = [\sum_j \Delta_j^2]^{1/2}$ exceeds γ_1, i.e.,

$$\Delta/\gamma_1 \gg 1. \tag{A1}$$

For the finite frequency components, all the modes correspond to the oscillatory motion, i.e., $\omega_j \gg \gamma_j$. The short-time (slow modulation) expansion is valid provided that

$$\Delta/\omega_j \gg 1; \quad (j = 2-L). \tag{A2}$$

Equations (A1) and (A2) ensure the applicability of the stochastic slow modulation limit for the emission line shapes. From the inspection of the parameters (Table VI), it is apparent that condition (A1) is well obeyed while condition (A2) is obtained for most of the finite frequency modes. In the slow modulation limit we have for the total emission linewidth $\Gamma_e = 2.355\,[\sum_j \Delta_j^2]^{1/2}$ resulting in Eq. (16).

[1] J. Jortner, Ber. Bunsen-Ges. Phys. Chem. **88**, 188 (1984).
[2] *The Chemical Physics of Atomic and Molecular Clusters*, Proceedings of the International School of Physics ''Enrico Fermi,'' edited by G. Scoles (North Holland, Amsterdam, 1990), Course CVII.
[3] R. S. Berry, J. Burdet, and A. W. Castleman, Z. Phys. D **26**, 1 (1993).
[4] J. Jortner, Z. Phys. **24**, 47 (1992).
[5] J. Jortner, J. Chim. Phys. **92**, 205 (1995).
[6] J. Jortner, U. Even, A. Goldberg, I. Schek, T. Raz, and R. D. Levine, Surf. Rev. Lett. **3**, 263 (1996).
[7] J. Stapelfeldt, J. Wörmer, and T. Möller, Phys. Rev. Lett. **62**, 98 (1989); T. Möller, Z. Phys. D **20**, 1 (1991).
[8] R. D. Evans, *The Atomic Nucleus* (McGraw-Hill, New York, 1955); A. Bohr and B. R. Mottelson, *Nuclear Structure* (Benjamin, New York, 1975), Vol. II.
[9] J. Wörmer, R. Karnbach, M. Joppien, and T. Möller, J. Chem. Phys. **104**, 8269 (1996).
[10] O. Björneholm, F. Federmann, F. Fossing, and T. Möller, Phys. Rev. Lett. **74**, 3017 (1995); O. Björneholm, F. Federman, F. Fösing, T. Möller, and S. Stampfli, J. Chem. Phys. **104**, 1876 (1996).
[11] M. Lengen, M. Joppien, R. Muller, J. Wörmer, and T. Möller, Phys. Rev. Lett. **68**, 2362 (1992).
[12] M. Lengen, M. Joppien, R. Pietrowski, and T. Möller, Chem. Phys. Lett. **229**, 362 (1994).
[13] M. Rutzen, S. Kakar, C. Reinecker, R. von Pietrowski, and T. Möller, Z. Phys. D **38**, 89 (1996).
[14] J. Wörmer and T. Möller, Z. Phys. D **20**, 39 (1991).
[15] A. Goldberg, A. Heidenreich, and J. Jortner, J. Phys. Chem. **99**, 2662 (1995).
[16] I. Messing, B. Raz, and J. Jortner, J. Chem. Phys. **66**, 2239 (1977).
[17] I. Messing, B. Raz, and J. Jortner, J. Chem. Phys. **66**, 4577 (1977).
[18] I. Messing, B. Raz, and J. Jortner, Chem. Phys. **23**, 23 (1977).
[19] J. Jortner, E. E. Koch, and N. Schwentner, *Electronic Excitations in Condensed Rare Gases*, Springer Tracts in Modern Physics 107 (Springer-Verlag, Heidelberg, 1985).
[20] A. Heidenreich and J. Jortner, J. Chem. Phys. **105**, 8523 (1996).
[21] D. Scharf and J. Jortner, Chem. Phys. Lett. **126**, 495 (1986).
[22] D. Scharf, J. Jortner, and U. Landman, J. Chem. Phys. **88**, 4273 (1988).
[23] J. Jortner, in *Femtochemistry, Chemistry and Physics of Ultrafast Processes in Molecular Systems*, edited by M. Chergui (World Scientific, Singapore, 1996), p. 15.
[24] L. E. Fried and S. Mukamel, Phys. Rev. Lett. **66**, 2340 (1991).
[25] L. E. Fried and S. Mukamel, J. Chem. Phys. **96**, 116 (1992).
[26] L. E. Fried and S. Mukamel, Adv. Chem. Phys. **26**, 217 (1993).
[27] S. Mukamel, J. Chem. Phys. **77**, 173 (1982).
[28] S. Mukamel, Phys. Rep. **93**, 1 (1982).
[29] R. Islampour and S. Mukamel, Chem. Phys. Lett. **107**, 239 (1984).
[30] R. Islampour and S. Mukamel, Chem. Phys. Lett. **80**, 5487 (1984).
[31] J. Sue, Y. J. Yan, and S. Mukamel, J. Chem. Phys. **85**, 462 (1986).
[32] S. Mukamel, *Principles of Nonlinear Optical Spectroscopy* (Oxford University Press, New York, 1995).
[33] A. Heidenreich and J. Jortner, Isr. J. Chem. **33**, 467 (1994).
[34] A. Heidenreich and J. Jortner, Z. Phys. D **26**, 377 (1993).
[35] D. Bahatt, A. Heidenreich, N. Ben-Horin, U. Even, and J. Jortner, J. Chem. Phys. **100**, 6290 (1994).
[36] A. Heidenreich, D. Bahatt, N. Ben-Horin, U. Even, and J. Jortner, J. Chem. Phys. **100**, 6300 (1994).
[37] P. Parneix, F. G. Amar, and Ph. Bréchignac, Z. Phys. D **26**, 217 (1993).
[38] T. Troxler and S. Leutwyler, Ber. Bunsen-Ges. Phys. Chem. **96**, 1246 (1992).
[39] G. N. Robertson and J. Yarwood, Chem. Phys. **32**, 267 (1978).
[40] W. G. Rothschild, J. Soussen-Jacob, J. Bessière, and J. Vincent-Geisse, Chem. Phys. **79**, 3002 (1983).
[41] D. Thiumalai, E. J. Bruskin, and B. J. Berne, J. Chem. Phys. **83**, 230 (1985).
[42] A. Rahman, Phys. Rev. **136**, 405 (1964).
[43] L. Verlet, Phys. Rev. **159**, 98 (1967).
[44] *Rare Gas Solids*, edited by M. L. Klein and J. A. Venables (Academic, London, 1976).
[45] M. P. Allen and D. G. Tildesley, *Computer Simulation of Liquids* (Clarendon, Oxford, 1992).
[46] F. H. Stillinger and T. A. Weber, Phys. Rev. A **25**, 978 (1982).
[47] F. H. Stillinger and T. A. Weber, Phys. Rev. A **28**, 2408 (1983).
[48] A. L. Mackay, Acta Crystallogr. **1**, 916 (1962).
[49] L. Perera and F. G. Amar, J. Chem. Phys. **93**, 4884 (1990).
[50] R. Kubo and Y. Toyozawa, Prog. Theor. Phys. **13**, 160 (1955).
[51] R. Kubo, Adv. Chem. Phys. **15**, 101 (1969).
[52] M. Rosenblit and J. Jortner, Phys. Rev. Lett. **75**, 4079 (1995).

[53] S. J. Rosenthal, X. Xie, M. Du, and G. R. Fleming, J. Chem. Phys. **95**, 4715 (1991).
[54] A. Migus, J. Martin, and A. Antonetti, Phys. Rev. Lett. **58**, 1559 (1987).
[55] E. Neria, A. Nitzan, R. N. Barnett, and U. Landman, Phys. Rev. Lett. **67**, 1011 (1991).
[56] J. Alfano, P. Wallhout, Y. Kimura, and P. Barbara, J. Chem. Phys. **98**, 5996 (1993).
[57] G. E. Uhlenbeck and L. S. Orenstein, Phys. Rev. **36**, 823 (1930).
[58] R. S. Berry, T. L. Beck, H. L. Davis, and J. Jellinek, Adv. Chem. Phys. **90**, 75 (1988).
[59] H. P. Cheng and R. S. Berry, Phys. Rev. A **45**, 7969 (1992).
[60] F. G. Amar and B. J. Berne, J. Chem. Phys. **88**, 6720 (1984).
[61] A. H. Zewail, *Femtochemistry* (World Scientific, Singapore, 1994).
[62] *Femtochemistry, Chemistry and Physics of Ultrafast Processes in Molecular Systems*, edited by M. Chergui (World Scientific, Singapore, 1996).
[63] M. Chergui, N. Schwentner, and V. Chandrasekharan, J. Chem. Phys. **89**, 1277 (1988).
[64] M. T. Portela-Oberli, C. Jeannin, and M. Chergui, Chem. Phys. Lett. **259**, 475 (1996).